
Massive star formation in W51A triggered by cloud-cloud collisions

Shinji FUJITA^{1,2,3*}, Kazufumi TORII³, Nario KUNO², Atsushi NISHIMURA¹,
Tomofumi UMEMOTO³, Tetsuhiro MINAMIDANI³, Mikito KOHNO¹,
Mitsuyoshi YAMAGISHI⁴, Tomoka TOSAKI⁵, Mitsuhiro MATSUO⁶, Yuya
TSUDA⁷, Kengo TACHIHARA¹, Akio OHAMA¹, Hidetoshi SANO¹,
Katsuhiro HAYASHI¹, Rei ENOKIYA¹, Satoshi YOSHIKE¹, Daichi
TSUTSUMI¹, Kazuki OKAWA¹, Yasuo FUKUI¹ and other FUGIN members

¹Department of Astrophysics, Nagoya University, Furo-cho, Chikusa-ku, Nagoya, Aichi, Japan
464-8602

²Department of Physics, Graduate School of Pure and Applied Sciences, University of
Tsukuba, 1-1-1 Ten-nodai, Tsukuba, Ibaraki, Japan 305-8577

³Nobeyama Radio Observatory, 462-2 Minamimaki, Minamisaku, Nagano, Japan 384-1305

⁴Institute of Space and Astronautical Science, Japan Aerospace Exploration Agency,
Chuo-ku, Sagamihara 252-5210, Japan

⁵Department of Geoscience, Joetsu University of Education, Joetsu, Niigata, Japan 943-8512

⁶Graduate Schools of Science and Engineering, Kagoshima University, 1-21-35 Korimoto,
Kagoshima, Kagoshima, Japan 890-0065

⁷Meisei University, 2-1-1 Hodokubo, Hino, Tokyo, Japan 191-0042

*E-mail: fujita.shinji@a.phys.nagoya-u.ac.jp

Received (reception date); Accepted (acceptation date)

Abstract

W51A is one of the most active star-forming regions in the Milky Way, which includes copious amounts of molecular gas with a total mass of $\sim 6 \times 10^5 M_{\odot}$. The molecular gas has multiple velocity components over $\sim 20 \text{ km s}^{-1}$, and interactions between these components have been discussed as the mechanism which triggered the massive star formation in W51A. In this pa-

per, we report an observational study of the molecular gas in W51A using the new ^{12}CO , ^{13}CO , and C^{18}O ($J=1-0$) data covering a $1.4^\circ \times 1.0^\circ$ area of W51A obtained with the Nobeyama 45-m telescope at $20''$ resolution. Our CO data resolved four discrete velocity clouds with sizes and masses of $\sim 30\text{ pc}$ and $1.0-1.9 \times 10^5 M_\odot$ around radial velocities of 50, 56, 60, and 68 km s^{-1} . Toward the central part of the HII region complex G49.5-0.4 in W51A, in which the bright stellar clusters IRS 1 and IRS 2 are located, we identified four C^{18}O clumps having sizes of $\sim 1\text{ pc}$ and column densities of higher than 10^{23} cm^{-2} , which are each embedded within the four velocity clouds. These four clumps are concentrated within a small area of 5 pc, but show a complementary distribution on the sky. In the position-velocity diagram, these clumps are connected with each others by bridge features having weak intensities. The high intensity ratios of ^{13}CO ($J=3-2$)/($J=1-0$) also indicate that these four clouds are associated with the HII regions including IRS 1 and IRS 2. We also revealed that, in the other bright HII region complex G49.4-0.3, the 50, 60, and 68 km s^{-1} clouds show a complementary distribution, with two bridge features connecting between the 50 and 60 km s^{-1} clouds and the 60 and 68 km s^{-1} clouds. An isolated compact HII region G49.57-0.27 located $\sim 15\text{ pc}$ north of G49.5-0.4 also shows a complementary distribution and a bridge feature. The complementary distribution on the sky and the broad bridge feature in the position-velocity diagram suggest collisional interactions among the four velocity clouds in W51A. The timescales of the collisions can be estimated to be several 0.1 Myrs as crossing times of the collisions, which are consistent with the ages of the HII regions measured from the sizes of the HII regions with the 21 cm continuum data. We discuss a scenario of the cloud-cloud collisions and massive star formation in W51A by comparing with the recent observational and theoretical studies of cloud-cloud collision.

Key words: ISM: clouds — ISM: individual objects (W51) — radio lines: ISM — stars: formation

1 Introduction

Massive stars are influential in the galactic environment by releasing heavy elements and a large amount of energy in ultra-violet (UV) radiation, stellar winds, outflows, and supernova explosions. It is therefore of fundamental importance to understand the mechanisms of massive star formation, and considerable efforts have been performed so far (e.g., Wolfire & Cassinelli 1987; Zinnecker & Yorke 2007; Tan et al. 2014). Theoretically, monolithic collapse (Yorke & Sonnhalter 2002; McKee & Tan

2003; Hosokawa et al. 2010) and competitive accretion (Bonnell et al. 2001; Bonnell et al. 2004; Wang et al. 2010) are the two actively-debated scenarios of the mass accretion processes to form massive stars, although these are still lack in convincing confrontation with the initial conditions provided by observations (Tan et al. 2014). It is therefore important to enlarge samples of giant molecular clouds (GMCs) by performing large-scale molecular line observations at high spatial resolution, since GMCs are the principal sites of massive star formation (e.g., Zinnecker & Yorke 2007). High spatial resolution less than 1 pc allows one to resolve the dense clumps embedded in GMCs, providing crucial information on the massive star formation.

W51 is one of the most active massive star-forming regions in the Milky Way (MW). It was discovered by the observations of the thermal radio continuum emission at 21 cm (Westerhout 1958). The distance to W51 was measured as 5.4 ± 0.3 kpc by Sato et al. (2010) based on the observations of trigonometric parallax, and the total far-infrared luminosity of W51 is as high as $\sim 8 \times 10^6 L_{\odot}$ at 5.4 kpc (Rengarajan et al. 1984). As shown in Figure 1, which shows a two color composite image of W51 with the *Spitzer* 8 and $24 \mu\text{m}$ data overlaid with the contour map of the 21 cm emission, W51 consists of a number of HII regions for a large area of $\sim 1^{\circ}$, which corresponds to ~ 100 pc at 5.4 kpc, and these HII regions are separated into two major groups, called W51A and W51B, at the northeastern and southwestern parts of W51, respectively (Bieging 1975). The total stellar masses included in W51A and W51B were measured as $1.8 \times 10^4 M_{\odot}$ and $1.4 \times 10^4 M_{\odot}$, respectively (Okumura et al. 2000; Kim et al. 2007). A supernova remnant W51C is located in the southeast, which can be traced in the non-thermal radio continuum emission (Koo & Moon 1997a; Koo & Moon 1997b). In this study, we focus on W51A, as it is a young massive star-forming region with ages of a few 0.1–1 Myrs (e.g., Kumar et al. 2004; Ginsburg et al. 2015), providing a unique opportunity to investigate the massive star formation in this remarkably bright star-forming region.

W51A harbors two bright HII region complexes, G49.5-0.4 and G49.4-0.3, which each include several HII regions within ~ 10 pc, as shown in the 21 cm continuum emissions in Figure 1(b). In G49.5-0.4, sixteen HII regions, named G49.5-0.4a–i, were identified (Mehringer 1994). The J , H , K' , and $\text{Br}\gamma$ photometric observations by Okumura et al. (2000) identified many O-type and early B-type stars toward these HII regions, as summarized in Table 1. The sizes of these HII regions ranges from ~ 0.1 pc to ~ 2 pc, which were used to estimate the ages of these HII regions to be 0.1–2.6 Myr (Okumura et al. 2000). The two outstanding radio sources G49.5-0.4e and G49.5-0.4d are also known as W51 IRS 1 and IRS 2 (Wynn-Williams et al. 1974), which each harbor 4–5 O-type stars and 2–4 early B-type stars, forming bright stellar clusters at the center of G49.5-0.4. The other sources G49.5-0.4a, b, c1, f, h, and i also have multiple O-type/early B-type stars. In addition to these HII regions, many massive young stellar objects (MYSOs) have been identified throughout G49.5-0.4 (Kang et al.

2009; Saral et al. 2017), indicating that massive star formation still continues in this region.

On the other hand, G49.4-0.3 consists of six HII regions G49.4-0.3 a–f with sizes of $\sim 0.7\text{--}2$ pc (Mehringer 1994). Although there is no photometric identifications of the exciting stars of these HII regions, their classifications were estimated to be O4–B0 as listed in Table 1 from the measurements of ionization photons with the 21 cm radio continuum data (Koo 1997). The typical age of the HII regions was measured as ~ 0.2 Myrs (see Section 5.1). Other than G49.5-0.4 and G49.4-0.3, there are several discrete HII regions within ~ 20 pc from G49.5-0.4 or G49.4-0.3, and the classifications of the exciting stars in these sources were measured as O4–B0 from the 21 cm data (see a summary in Table 1).

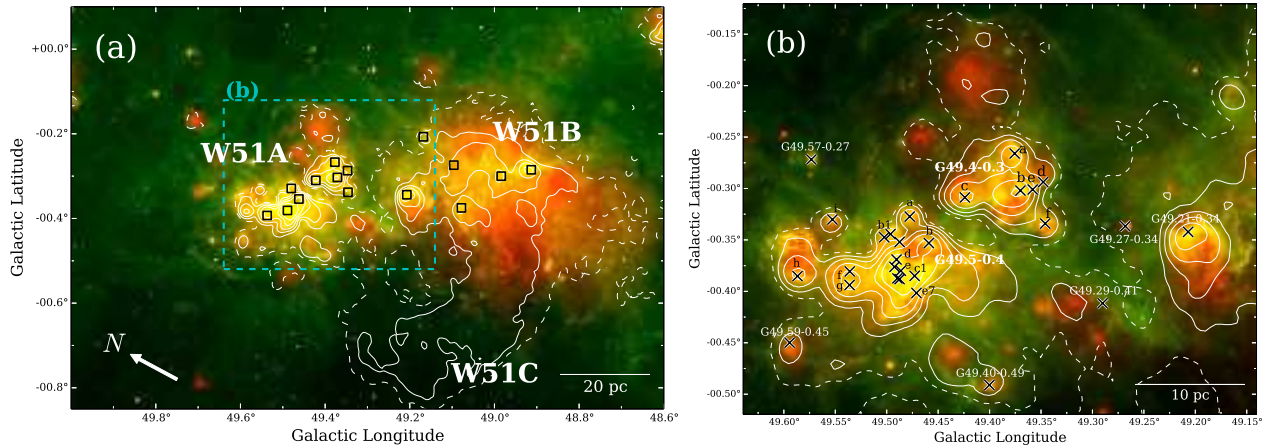


Fig. 1: (a) A composite color image of the *Spitzer*/MIPSGAL $24\ \mu\text{m}$ (red) and *Spitzer*/GLIMPSE $8\ \mu\text{m}$ (green) emissions toward W51. The white contours indicate the VGPS 21 cm radio continuum emission (Stil et al. 2006), and are plotted at 25 (dashed lines), 50, 100, 200, 400, and 800 K (solid lines). Square symbols represent the compact radio continuum sources identified by Koo (1997). (b) A close-up view of W51A. The corresponding region is indicated by the box with dashed blue lines in (a). Crosses represent the HII regions listed in Mehringer (1994) (see also Table 1).

Molecular gas in W51 shows an extended distribution for $\sim 100\ \text{pc} \times 100\ \text{pc}$, with a total molecular mass measured as $\sim 7.1 \times 10^5 M_{\odot}$ at 5.4 kpc (Carpenter & Sanders 1998). The CO emissions in W51A has multiple velocity components in a radial velocity range between $\sim 50\text{--}70\ \text{km s}^{-1}$. Based on the large scale ^{12}CO and ^{13}CO ($J=1\text{--}0$) observations covering the entirety of the W51 region at an angular resolution of $46''$, Carpenter & Sanders (1998) decomposed the velocity structures of molecular gas by performing fits to the CO spectra with multiple Gaussian functions. Subsequently, Okumura et al. (2001) performed ^{13}CO ($J=1\text{--}0$) observations at a high angular resolution of $15''$ toward a $\sim 15' \times 15'$ area centered on G49.5-0.4. By analyzing the position-velocity diagrams, the authors identified four velocity components around radial velocities of 50, 56, 60, and $68\ \text{km s}^{-1}$.

The 68 km s^{-1} cloud corresponds to High Velocity Stream (HVS), which is a filamentary molecular cloud stretched nearly parallel to the Galactic plane, overlapping W51A and W51B along the line-of-sight. The length and width of HVS were measured as $\sim 100 \text{ pc}$ and $\sim 10 \text{ pc}$, respectively (Carpenter & Sanders 1998; Kang et al. 2010; Parsons et al. 2012). Burton & Shane (1970) and Koo (1999) discussed that the large velocity of HVS is attributed to the streaming motion of gas down to the Sagittarius spiral arm driven by the spiral density wave. For the velocity components other than HVS, Carpenter & Sanders (1998) discussed that these represent kinematic structures within a single molecular cloud, the W51 cloud, with a total molecular mass of $\sim 6.0 \times 10^5 M_{\odot}$, refereed as the W51 cloud, whereas Okumura et al. (2001) postulated that these are discrete molecular clouds located at the same distance.

It has been actively debated that the massive star formation in W51A was triggered by collisions between molecular clouds having different radial velocities over $\sim 20 \text{ km s}^{-1}$ (Pankonin et al. 1979; Arnal & Goss 1985; Carpenter & Sanders 1998; Koo 1999; Okumura et al. 2001). Carpenter & Sanders (1998) proposed a collision between the W51 cloud and HVS. The authors revealed that the CO emissions around 60 km s^{-1} in the W51 cloud truncates at the location of HVS, and discussed that these two velocity components are physically related objects at a common distance, suggesting a collision between these two clouds. Kang et al. (2010) reached to the same conclusion, based on the ^{12}CO and ^{13}CO ($J=2-1$) observations at $36''$ resolution, which covered a $1.^{\circ}25 \times 1.^{\circ}00$ area of W51. Okumura et al. (2001) argued a “pileup” scenario of the four discrete molecular clouds, resulted in a burst of massive star formation in G49.5-0.4 in W51A.

Recently, supersonic collision between molecular clouds has been discussed as a plausible mechanism of massive star formation. These observational studies of cloud-cloud collisions (CCCs) include the super star clusters and the HII regions in the MW and young O stars in the Large Magellanic Cloud (Fukui et al. 2014; Fukui et al. 2015; Fukui et al. 2017b; Fukui et al. 2017c; Furukawa et al. 2009; Hayashi et al. 2017; Kohno et al. 2017; Nishimura et al. 2017a; Nishimura et al. 2017b; Ohama et al. 2010; Ohama et al. 2017a; Ohama et al. 2017b; Sano et al. 2017; Shimoikura et al. 2013; Torii et al. 2011; Torii et al. 2015; Torii et al. 2017a; Torii et al. 2017b; Tsuboi et al. 2015; Takahira et al. 2017; Tsutsumi et al. 2017), where the super star clusters include 10–20 O stars, while the others with a single young O star. Formation of the massive clumps, which may form massive stars, in the collisional-compressed layer was discussed in depth in the magneto-hydrodynamical (MHD) simulations by Inoue & Fukui (2013) and Inoue et al. (2017). Kobayashi et al. (2017) formulated the time evolution equation of GMC mass function including CCC, indicating that CCC-driven star formation is mostly driven by massive GMCs having masses $> 10^{5.5} M_{\odot}$, which may account for a few 10% of the total star formation in the MW and nearby

galaxies. Comparisons between the observations and numerical calculations have indicated two important observational signatures of CCCs, i.e., “broad bridge feature” in position-velocity diagrams and “complementary distribution” on the sky between two molecular clouds with different velocities, which provide useful diagnostics to investigate CCCs with molecular line observations (Habe & Ohta 1992; Anathpindika 2010; Takahira et al. 2014; Torii et al. 2017a; Fukui et al. 2017b).

Following the recent improvement of our knowledge on CCC as a trigger of massive star formation, in this study we present an analysis of the new ^{12}CO , ^{13}CO , and C^{18}O ($J=1-0$) data covering the entirety of W51A in order to test the CCC model as the mechanism of the active massive star formation in W51A. The CO data was obtained using the Nobeyama 45-m telescope at $20''$ resolution, which corresponds to ~ 0.5 pc at 5.4 kpc, as a part of the Galactic plane survey legacy project FUGIN (FOREST Unbiased Galactic plane Imaging survey with the Nobeyama 45-m telescope) (Minamidani et al. 2016; Umemoto et al. 2017). The advantages of our new CO ($J=1-0$) data can be summarized as follows:

1. We covered a large area of 1.4×1.0 including W51A at a comparable spatial resolution with that in the ^{13}CO ($J=1-0$) observations by Okumura et al. (2001), which covered a $\sim 15' \times 15'$ area of G49.5-0.4.
2. Our data includes the C^{18}O ($J=1-0$) emission, which allows us to diagnose the signatures of CCCs in the molecular clouds in W51A. Note that the C^{18}O ($J=1-0$) emission has not been studied for a large area of W51A at such a high angular resolution. Parsons et al. (2012) performed a large-scale ^{12}CO , ^{13}CO , and C^{18}O ($J=3-2$) observations with the JCMT telescope toward W51A and W51B, providing a comprehensive catalog of the dense gas in the molecular clouds in W51A. However, the authors did not focus on the spatial and velocity distributions of gas at an aim of investigating interactions among different velocity components.
3. Our CO data has a comparable spatial resolution with the JCMT archival CO ($J=3-2$) data (Parsons et al. 2012), allowing us to investigate the excitation conditions of gas, and to probe interaction between molecular gas and HII regions.

In Section 2 we summarize recent studies of the CCC regions and introduce the observational signatures characteristic to CCC. In Section 3 we describe the CO dataset used in this study, and in Section 4 we present the main results of the analyses on the CO dataset and comparisons with the other wavelengths. In Section 5 we discuss the results, and a summary is presented in Section 6.

2 Observational signatures of CCC

Based on comparisons between observations and simulations, Fukui et al. (2017b) and Torii et al. (2017a) discussed two possible observational signatures of CCC, i.e., “broad bridge feature” in position-velocity diagrams and “complementary distribution” on the sky between two clouds with different velocities, where the authors assumed a collision between two dissimilar clouds based on the basic CCC model studied by Habe & Ohta (1992), followed by Anathpindika (2010); Takahira et al. (2014); Haworth et al. (2015a); Haworth et al. (2015b); Takahira et al. (2017). Broad bridge feature is relatively weak CO emissions at intermediate velocities between two colliding clouds that are separated in velocity. When a smaller cloud drives into a larger cloud, a dense compressed layer at the collisional interface is formed, resulting in a thin turbulent layer between the larger cloud and the compressed layer. If one observes a snapshot of this collision with a viewing angle parallel to the colliding axis, two velocity peaks separated by intermediate-velocity emission with lower intensity can be seen in the position-velocity diagrams. The turbulent gas which create the broad bridge feature can be replenished as long as the collision continues. Several observational studies reported detections of broad bridge features in the CCC regions (e.g., Fukui et al. 2014; Fukui et al. 2016; Fukui et al. 2017a; Furukawa et al. 2009; Ohama et al. 2010; Torii et al. 2015; Torii et al. 2017a).

When two clouds collides, one caves the other owing to the momentum conservation (Haworth et al. 2015b). If the collision takes place head-on between two dissimilar clouds, a cavity will be formed on the larger cloud through this process, and the larger cloud can be seen as a ring-like structure on the sky, unless the observer viewing angle is perfectly perpendicular to the colliding axis. As the size of the cavity corresponds to that of the smaller cloud, the observer with a viewing angle parallel to the colliding axis sees a complementary distribution between the smaller cloud and the ring-like structure of the larger cloud. If the collision is an offset collision, not a head-on collision, the basic process is not changed, and two clouds with different velocities can be observed close to each other. These two clouds may share the boundaries of the clouds on the sky, showing a complementary distribution. Fukui et al. (2017b) and Fukui et al. (2017c) pointed out that if the observer viewing angle has an inclination relative to the colliding axis, the complementary distribution has a spatial offset depending on the travel distance of the collision or the depth of the cavity.

In the well-resolved CCC regions, a combination of the two signatures of CCC, broad bridge feature and complementary distribution, may be observed as a “V-shape” gas distribution in the p - v diagram (e.g., Fukui et al. 2017b; Ohama et al. 2017b; Hayashi et al. 2017; Torii et al. 2017b). Analyses of the synthetic CO data by Fukui et al. (2017b) indicate that, if the observer viewing angle is inclined relative to the colliding axis, the V-shape distribution becomes skew.

In this study, using the new CO ($J=1-0$) dataset, we investigate these observational signatures of CCC in the molecular clouds in W51A. We also utilize the CO ($J=3-2$) data to take intensity ratios between $J=3-2$ and $J=1-0$ transitions of CO, which provides a useful tool to investigate the physical condition of molecular gas. In the previous studies of the CCC regions, intensity ratios between different J transitions of CO were used to diagnose associations of the two velocity clouds with the HII regions (e.g., Torii et al. 2011; Fukui et al. 2014; Torii et al. 2015; Fukui et al. 2016; Hayashi et al. 2017), as molecular gas situated close to HII regions is heated up by the UV radiation, resulting in high intensity ratios of gas.

3 Dataset

The observations of W51A were carried out as a part of FUGIN project (Umemoto et al. 2017). Details of the observations, calibration, and data reduction are summarized in Umemoto et al. (2017), and parameters of the observations and output data are listed in Table 2. In W51A, we covered a $l = 50^{\circ}0-48^{\circ}6$, $b = -0^{\circ}9-+0^{\circ}1$ (1.4×1.0) in the ^{12}CO ($J=1-0$), ^{13}CO ($J=1-0$), C^{18}O ($J=1-0$) emissions. The SAM45 (Spectral Analysis Machine for the 45-m telescope) spectrometer (Kuno et al. 2011) was used at a frequency resolution of 244.14 kHz, and the effective velocity resolution was 1.3 km s^{-1} at 115 GHz. The typical system noise temperatures including atmosphere were $\sim 150 \text{ K}$ and $\sim 250 \text{ K}$ at 110 GHz and 115 GHz, respectively. The output cube data has spatial grids of $8.5'' \times 8.5''$ and velocity grid of 0.65 km s^{-1} at an effective angular resolution of $20''$. The final root-mean-square (r.m.s) noise temperature T_{rms} are 1.5 K, 0.7 K, and 0.7 K in T_{mb} scale for ^{12}CO ($J=1-0$), ^{13}CO ($J=1-0$), C^{18}O ($J=1-0$), respectively.

The ^{13}CO ($J=3-2$) data was obtained by Parsons et al. (2012) with the Heterodyne Array Receiver Programme (HARP) receiver and the back-end digital autocorrelator spectrometer Auto-Correlation Spectral Imaging System (ACSIS) on the James Clerk Maxwell Telescope (JCMT). The observations covered a $1.4^{\circ} \times 1.0^{\circ}$ area including W51A and W51B. The data has an angular resolution of $14''$ at a velocity resolution of 0.5 km s^{-1} .

Table 1: List of the HII regions and massive stars in W51A

Name	Diameter (pc)	$\log N_i$ (photons/sec)	Classification	Age (Myr)	Reference
(1)	(2)	(3)	(4)	(5)	(6)
G49.21-0.34	~6.7	49.8	[O4]	1.1*	[1]
G49.27-0.34	<0.7	45.6	[B0]	<0.3*	[1]
G49.29-0.41	<0.7	47.3	[B0]	<0.1*	[1]
G49.4-0.3 a	~1.4×1.0	49.0	[O6]	0.1*	[1, 2]
... b	~2.1	49.7	[O5]	0.2*	[1, 2]
... c	~2.4×1.4	49.3	[O5.5]	0.2*	[1, 2]
... d	~4.8	48.6	[O7]	1.2*	[1, 2]
... e	<0.7	47.7	[O9.5]	<0.1*	[1, 2]
... f	~1.9	48.2	[O8.5]	0.3*	[1]
G49.40-0.49	<0.7	48.2	[O8.5]	<0.1*	[1]
G49.5-0.4 a	~1.4	49.0	O5+B1	0.7	[1, 2, 3]
... b	~1.0×0.5	49.6	O4+O8+B0	2.2	[1, 2, 3]
... b1	~1.2	48.2	O9	0.8	[1, 3]
... b2	~0.1	47.3	B1	0.2	[1, 3]
... b3	~0.7	48.1	[O9]	-	[1]
... c1	~1.9	49.2	O5+O6+B0	0.4	[1, 3]
... d (IRS 2)	~0.2	49.7	O4+O6×4+B0+B1×3	0.1	[1, 3]
... e (IRS 1)	...	50.4	O4+O5+O6+O8+B0×2	-	[1, 2, 3]
... e1	≤0.1	47.9	[O9.5]	-	[1]
... e2	≤0.1	>47.6	[>B0]	-	[1]
... e6	≤0.1	47.3	[B0]	-	[1]
... e7	~0.3×0.2	47.2	B0	0.3	[1, 3]
... f	~1.4×0.7	49.1	O7+B0+B1×2	1.8	[1, 2, 3]
... g	~0.7	48.9	[O5×2+B1]	1.5	[2]
... h	~2.4×1.4	48.9	O5+B0×4+B1	2.6	[1, 2, 3]
... i	~1.0	48.4	O8+B1	1.5	[1, 3]
G49.57-0.27	≤0.7	47.5	[B0]	≤0.1*	[1]
G49.59-0.45	~4.8×2.9	48.7	[O7]	0.8*	[1]

(1) Name of the HII region. (2) Diameter of the HII region measured at 10% of the maximum intensity of the radio continuum emissions (Mehring 1994). (3) Ionizing photon flux estimated by Mehringer (1994). (4) Classification of the exciting stars in the HII region estimated by Mehringer (1994) and Okumura et al. (2000). Those derived by measuring ionizing photons from radio continuum image is shown with brackets, while those identified in the near-infrared photometric observations are presented without brackets. (5) Expansion age of the HII region estimated by Mehringer (1994) or in this study. Those with asterisk were measured in this study (see Section 5.1). (6) References. [1] Mehringer (1994), [2] Koo (1997), [3] Okumura et al. (2000).

Table 2: Summary of the CO ($J=1-0$) dataset

Observation Date	March – May 2014 and April – May 2015
Observed Area	$l = 50^{\circ}0-48^{\circ}6$, $b = -0^{\circ}9-+0^{\circ}1$ ($1^{\circ}4 \times 1^{\circ}0$)
Telescope	NRO 45-m telescope
Receiver	FOREST
Observation Mode	On-The-Fly
Emission Lines	^{12}CO ($J=1-0$), ^{13}CO ($J=1-0$), and C^{18}O ($J=1-0$)
Angular and Velocity Resolution	$\sim 20''$ (~ 0.5 pc for distance 5.4 kpc) and $\sim 1.3 \text{ km s}^{-1}$
Angular and Velocity Grid of the final cube data	$8.5''$ and 0.65 km s^{-1}
T_{rms}	~ 1.5 K for ^{12}CO ($J=1-0$), ~ 0.7 K for ^{13}CO ($J=1-0$), and ~ 0.7 K for C^{18}O ($J=1-0$)

4 Results

4.1 Large-scale gas distribution

4.1.1 CO ($J=1-0$) distribution

Figure 2 shows the v - b diagram of the ^{13}CO ($J=1-0$) emissions for $l = 49.^\circ55-49.^\circ25$, which covers the W51A region shown in Figure 1(b). Four velocity components identified in the previous studies can be seen as indicated as vertical dotted lines (Okumura et al. 2001), and it can be seen that these clouds are connected with each others by the intermediate velocity emissions. Following the nomenclature by Okumura et al. (2001), we hereafter refer the velocity components around 50, 56, 60, and 68 km s^{-1} as “the 50 km s^{-1} cloud”, “the 56 km s^{-1} cloud”, “the 60 km s^{-1} cloud”, and “the 68 km s^{-1} cloud (HVS)”, respectively.

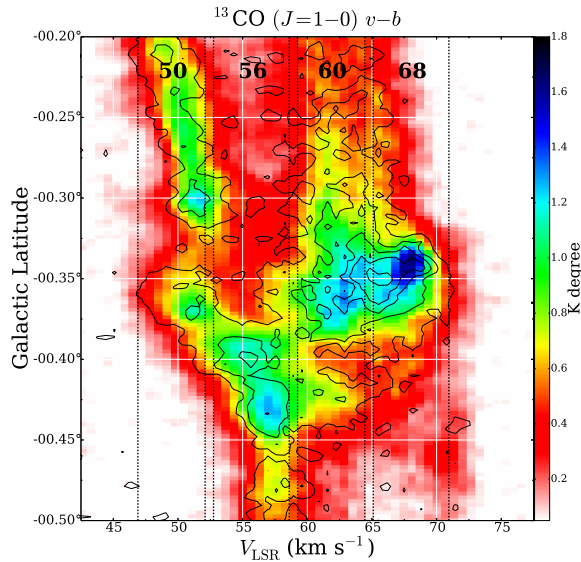


Fig. 2: The Velocity–Galactic Latitude ($v - b$) diagram of the ^{13}CO and C^{18}O ($J=1-0$) emissions integrated over $l = 49.^\circ55 - 49.^\circ25$, where the color shows ^{13}CO and the contours plotted at every 0.06 K degree from 0.06 K degree show C^{18}O . The vertical dotted lines indicate the velocity ranges of the four velocity clouds shown in Figures 3–5.

Figures 3–5 show the ^{12}CO , ^{13}CO and C^{18}O ($J=1-0$) integrated intensity distributions of the four velocity clouds, respectively, overlaid with the contour map of the 21 cm radio continuum data (Stil et al. 2006). We also present the velocity channel maps of the ^{12}CO , ^{13}CO , and C^{18}O emissions in Figures 12–14 in the appendix for supplements. The ^{12}CO emissions presented in Figure 3 show extended gas distributions of the four clouds, while the ^{13}CO emissions show that the clouds have networks of clumpy and filamentary structures. C^{18}O probes only clumpy structures except for the

68 km s⁻¹ cloud.

The 50 km s⁻¹ cloud shown in the panel (a) in Figures 3–5 has strong intensity peaks toward G49.5-0.4 and G49.4-0.3. In the ¹³CO emissions these peaks are connected with each others with filamentary structures roughly elongated along the northeast-southwest direction at $b \sim -0^\circ.38$ – $-0^\circ.32$ (Figure 4(a)), which are not apparent in the ¹²CO emissions (Figure 3(a)), whereas the C¹⁸O emissions show fragmented distributions with sizes of ~ 2 – 3 pc toward these peaks (Figure 5(a)). We derived the total molecular mass of the 50 km s⁻¹ cloud as $\sim 1.1 \times 10^5 M_\odot$ using the ¹³CO ($J=1-0$) map in Figure 4(a) with an assumption of the local thermodynamic equilibrium (LTE). We adopted an abundance ratio [¹³CO]/[H₂] of 1.5×10^{-6} (Dickman 1978) and a uniform excitation temperature (T_{ex}) of 15 K, which was measured from the average value of the peak brightness temperature of the optically-thick ¹²CO ($J=1-0$) emissions in the 50 km s⁻¹ cloud. We confirmed that the derived column densities are not significantly changed with T_{ex} between 10 K and 20 K (Schneider et al. 2016).

The CO emissions in the 56 km s⁻¹ cloud shown in the panel (b) in Figures 3–5 are enhanced at $(l, b) \sim (49^\circ.48, -0^\circ.40)$ in G49.5-0.4, whose CO intensities are strongest among the four velocity clouds in W51A. The ¹³CO emissions show filamentary structures, and some of them are radially elongated from the CO peak at G49.5-0.4 (Figure 4(b)), while the C¹⁸O emission is detected only toward the peak with a size of ~ 3 pc (Figure 5(b)). The total molecular mass of the 56 km s⁻¹ cloud measured using the ¹³CO map in Figure 4(b) is $\sim 1.3 \times 10^5 M_\odot$.

The 60 km s⁻¹ cloud in the panel (c) in Figures 3–5 shows similar gas distribution as the 56 km s⁻¹ cloud, as in the ¹³CO emissions it consists of a strong CO peak at G49.5-0.4, attached with filamentary structures (Figure 4(c)). A difference between the 50 and 56 km s⁻¹ clouds is the diffuse ¹³CO emissions extended above $b \sim -0^\circ.3$ between l of $49^\circ.45$ and $49^\circ.30$. The total molecular mass of the 60 km s⁻¹ cloud estimated with the ¹³CO map is as large as $\sim 1.9 \times 10^5 M_\odot$. The C¹⁸O distribution in Figure 5(c) is highly fragmented in G49.5-0.4 and G49.4-0.3. Note that the C¹⁸O fragments distributed to the east of G49.4-0.3 at $(l, b) \sim (49^\circ.38, -0^\circ.32)$ corresponds to a part of the ¹³CO filamentary structure which surrounds the 21 cm contours of G49.4-0.3 (Figure 4(c)), suggesting possible interaction between the 60 km s⁻¹ cloud and G49.4-0.3.

In the panel (d) in Figures 3–5, the 68 km s⁻¹ cloud has a filamentary structure elongated nearly parallel to the galactic plane between l of $49^\circ.50$ and $49^\circ.20$. The width of the filament can be measured as ~ 4 – 8 pc in the ¹²CO and ¹³CO emissions, while it is thinner in the C¹⁸O emissions, ~ 3 pc. The northeastern tip of the filament is spatially coincident with G49.5-0.4, while the opposite end corresponds to the HII region G49.21-0.34. The total mass of the 68 km s⁻¹ cloud is estimated as $\sim 1.3 \times 10^5 M_\odot$, which is consistent with the estimate in Carpenter & Sanders (1998).

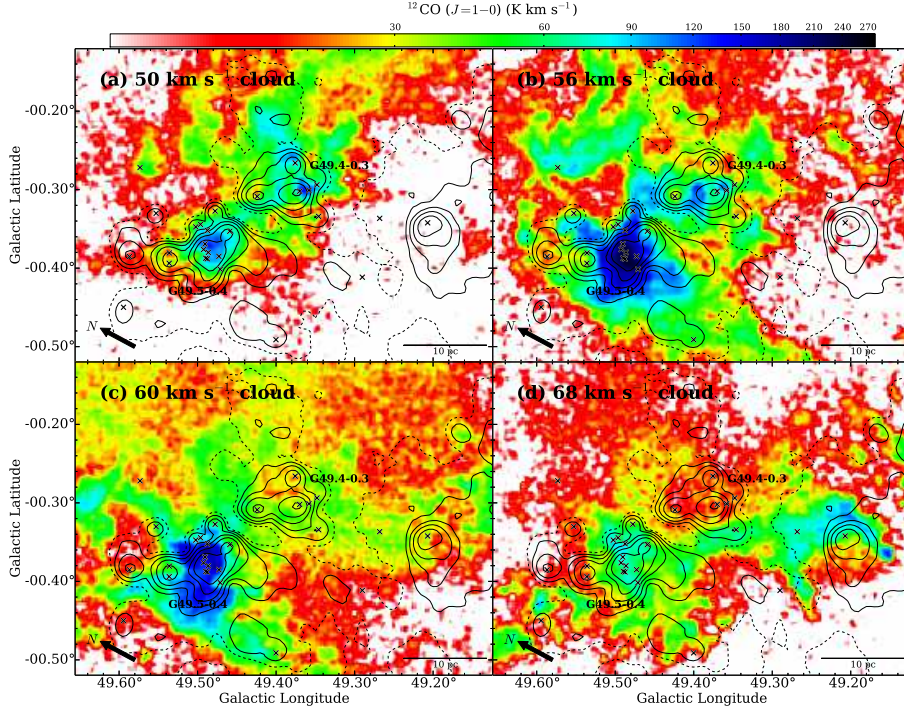


Fig. 3: The ^{12}CO ($J=1-0$) integrated intensity distributions of the (a) 50, (b) 56, (c) 60, and (d) 68 km s^{-1} clouds, with the integration ranges of $46.9-52.1$, $52.8-58.6$, $59.3-64.5$, and $65.1-71.0 \text{ km s}^{-1}$, respectively (see also the dotted lines in Figure 2). Contours show the 21 cm radio continuum emissions (Stil et al. 2006), and are plotted at 25 (dashed lines), 50, 100, 200, 400, and 800 K, while rosses represent HII regions listed in Mehringer (1994).

4.1.2 CO ($J=3-2/J=1-0$) intensity ratios

Figures 6(a)–(d) show large-scale distributions of the ^{13}CO ($J=3-2$)/ ^{13}CO ($J=1-0$) intensity ratios (hereafter R_{3210}^{13}) of the four clouds in W51A. The four clouds typically have R_{3210}^{13} of higher than 0.6, up to over 2.0, while low R_{3210}^{13} less than 0.2 is seen in the diffuse gas widely distributed at $b > -0^\circ.30$ – $-0^\circ.20$ and $b < -0^\circ.45$. In order to extract the molecular gas heated up by the massive stars in W51A, in Figures 6(e)–(h) we plot the ^{13}CO ($J=1-0$) contour maps of the four clouds using only the voxels having R_{3210}^{13} of higher than 1.0. In Appendix 2, we performed the large velocity gradient (LVG) analysis, indicating that R_{3210}^{13} of higher than 1.0 can probe the high-temperature gas having $> 20 \text{ K}$.

In G49.5-0.4, the high- R_{3210}^{13} gas is seen in all of the four clouds, and physical associations between these clouds and the HII regions in G49.5-0.4 are thus suggested. In G49.4-0.3, on the other hand, the filamentary structures seen in the $8 \mu\text{m}$ image are well traced by the high- R_{3210}^{13} gas in the 50 km s^{-1} cloud, forming an arch-like gas distribution (Figures 6(a) and (e)). The 56 km s^{-1} cloud is also high in R_{3210}^{13} at the footpoints of the arch-like structure (Figures 6(b) and (f)). In the 60 km s^{-1} cloud, high- R_{3210}^{13} gas look surrounding the eastern and southeastern rim of the 21 cm emissions of

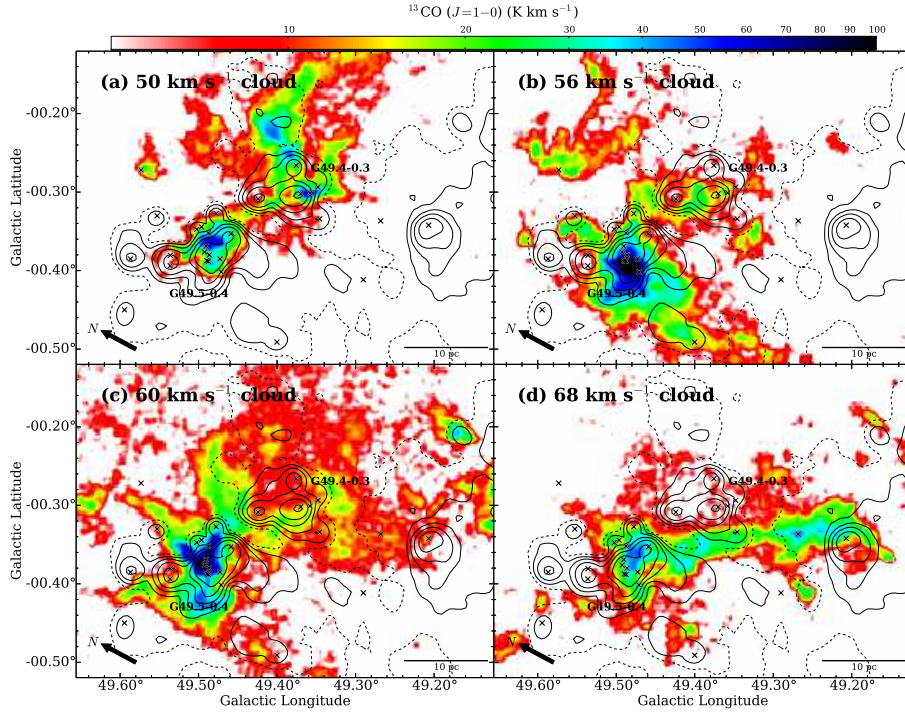


Fig. 4: Same as Figure 3 but for the ^{13}CO ($J=1-0$) emissions.

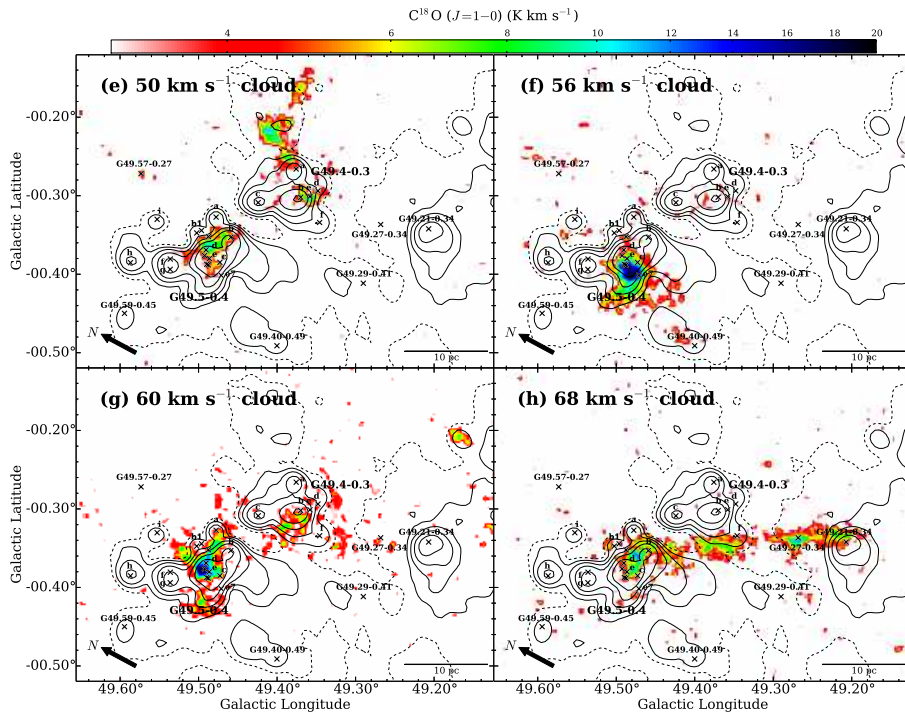


Fig. 5: Same as Figure 3 but for the C^{18}O ($J=1-0$) emissions.

G49.4-0.3 (Figures 6(c) and (g)). The 68 km s^{-1} cloud show continuous distribution of high- R_{3210}^{13} gas between the east and the south of G49.4-0.3, although its association with G49.4-0.3 is not clear (Figures 6(d) and (h)). These results indicate physical associations of multiple velocity components of gas with G49.5-0.4 and G49.4-0.3.

Associations of the other HII regions with the multiple velocity components can also be investigated in Figures 6(e)–(h). G49.57-0.27 is an isolated HII region situated at the north of G49.5-0.4, which shows high R_{3210}^{13} in the 50 and 56 km s^{-1} clouds (Figures 6(e) and (f)). There are several relatively expanded HII regions in G49.5-0.4, i.e., G49.5-0.4f, g, h, and i. Although we found no high- R_{3210}^{13} gas spatially overlapping these HII regions, there are several high- R_{3210}^{13} components in the 50 , 56 , and 60 km s^{-1} clouds which are distributed at the rims of the 21 cm continuum emissions of these HII regions (Figures 6(e)–(g)). As these four HII regions are relatively evolved with ages of an order of 1 Myr as summarized in Table 1, these high- R_{3210}^{13} gas can be interpreted as the remnants of the natal molecular gas of the massive stars in these HII regions. In the other HII regions, we found no plausible signatures of physical association of multiple velocity components. These show either no high- R_{3210}^{13} gas in the four clouds (e.g., G49.29-0.41) or high- R_{3210}^{13} gas only in one cloud (e.g., G49.21-0.34, G49.27-0.34, and G49.59-0.45). In the next subsection, we present the detailed gas distribution toward the individual HII regions which are likely associated with multiple velocity clouds.

4.2 Detailed gas distributions toward individual HII regions

4.2.1 G49.5-0.4

Figure 7 shows a close-up view of G49.5-0.4 with comparisons between the *Spitzer* $8 \mu\text{m}$ image (Carey et al. 2009) and the C^{18}O contour maps of the four clouds, where the HII regions listed in Table 1 are depicted by crosses, and the MYSOs identified by Saral et al. (2017) are plotted with triangles. The $8 \mu\text{m}$ emission is bright around $(l, b) \sim (49^\circ 45' - 49^\circ 49', -0^\circ 40' - -0^\circ 33')$, at which many compact HII regions including IRS 1 (G49.5-0.4e) and IRS 2 (G49.5-0.4d) are concentrated. Figure 7 shows that the four clouds have compact and bright C^{18}O emissions within a few pc of the central $8 \mu\text{m}$ structure.

We identified C^{18}O clumps in this region by drawing a contour at the 70% level of the maximum integrated intensity in the four clouds, resulted in discoveries of the four C^{18}O clumps which are each embedded within the four clouds. The results are summarized in Table 3. The peak column densities of the four clumps in the 50 , 56 , 60 , and 68 km s^{-1} clouds are measured as 2.6 , 5.4 , 4.9 , and $2.9 (\times 10^{23}) \text{ cm}^{-2}$, respectively, from the C^{18}O ($J=1-0$) data by assuming LTE and a uniform T_{ex} of

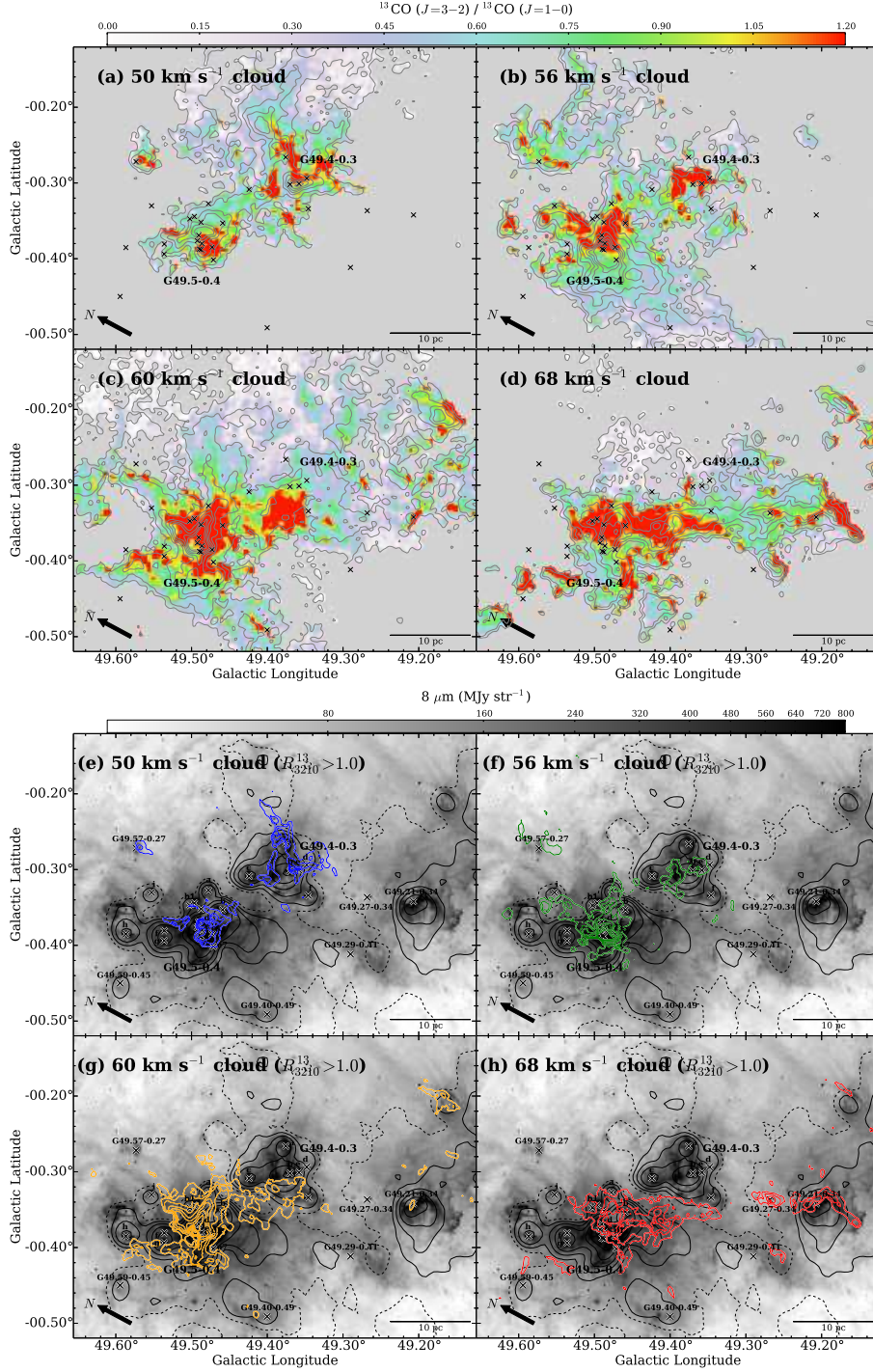


Fig. 6: (a–d) R_{3210}^{13} distributions of the four clouds. Contours indicate $^{13}\text{CO} (J=1-0)$, and are plotted at every 10 K km s^{-1} from 10 K km s^{-1} for the 50, 56, and 60 km s^{-1} clouds and at every 8 K km s^{-1} from 8 K km s^{-1} for the 68 km s^{-1} cloud. (e–h) Spatial distributions of the high- R_{3210}^{13} gas are shown in the colored contour maps, where the high- R_{3210}^{13} data was made by integrating only the voxels having $R_{3210}^{13} > 1.0$. The colored contours are plotted at the same levels as in (a)–(d). The background image indicates the *Spitzer* $8 \mu\text{m}$ image, while the black contours represent the 21 cm continuum emissions plotted at the same levels as those in Figure 3. Crosses are the same as those in Figure 3.

15 K. We here adopted an abundance ratio of $[C^{18}O]/[H_2] = 1.7 \times 10^{-7}$ (Frerking et al. 1982).

Figure 8(a) shows comparisons of the identified four $C^{18}O$ clumps superimposed on the *Spitzer* $8 \mu\text{m}$ image, where the $C^{18}O$ ($J=1-0$) contours are plotted at 60, 70, 80, and 90 % of the peak intensities of the clumps. Although these four clumps are concentrated within a small area of less than 5 pc, These are not spatially coincident along the line-of-sight, showing a complementary distribution. The complementary distribution between the 60 and 68 km s^{-1} clouds was discussed by Carpenter & Sanders (1998) based on their CO observations, and a CCC scenario between these two clouds were suggested by the authors. Our CO data newly revealed that the complementary distribution are seen not only for the 60 and 68 km s^{-1} clouds, but also for all of the four clouds.

The compact HII regions depicted by crosses are distributed around the rims of these four clumps. IRS 2 (G49.5-0.4d) is distributed at the interface of the clumps between the 50 and 60 km s^{-1} clouds, while IRS 1 (G49.5-0.4e) is seen at the boundaries of the 56, 60, and 68 km s^{-1} clouds. The other HII regions G49.5-0.4e1, e2, and e6 also are distributed at the interface of the four clouds, where the $8 \mu\text{m}$ emission is also enhanced (Figure 8(a)). The v - b diagram of the ^{13}CO and $C^{18}O$ ($J=1-0$) emissions shown in Figure 8(b) indicates that the four clumps are connected with each others by the CO emissions with intermediate intensities. These intermediate velocity features are possibly interpreted as the broad bridge features crated in CCC process as discussed in Section 2.

Table 3: Parameters of the $C^{18}O$ ($J=1-0$) clumps in G49.5-0.4

cloud name	peak position and peak velocity (l, b, v_{LSR})	radius (pc)	mass ($10^4 M_{\odot}$)	$N_{\text{max}}(\text{H}_2)$ (10^{23} cm^{-2})
(1)	(2)	(3)	(4)	(5)
50 km s^{-1} cloud	$49^{\circ}492, -0^{\circ}365, 51.1 \text{ km s}^{-1}$	~ 1.1	0.9	2.6
56 km s^{-1} cloud	$49^{\circ}485, -0^{\circ}400, 54.4 \text{ km s}^{-1}$	~ 1.1	2.5	5.4
60 km s^{-1} cloud	$49^{\circ}495, -0^{\circ}379, 61.5 \text{ km s}^{-1}$	~ 0.8	1.0	4.9
68 km s^{-1} cloud	$49^{\circ}473, -0^{\circ}360, 66.1 \text{ km s}^{-1}$	~ 1.0	1.1	2.9

(1) Name of the cloud in which the clump is embedded. (2) Peak position of the $C^{18}O$ ($J=1-0$) integrated intensity. (3) Radius of the clump, which was measured at 70% of the peak intensity of the clump. (4) Molecular mass derived from $C^{18}O$ ($J=1-0$) intensity maps assuming LTE with T_{ex} of 15 K. (5) Maximum H_2 column density of the clump.

4.2.2 G49.4-0.3

Figure 9 shows the ^{13}CO ($J=1-0$) contour maps of the four clouds toward G49.4-0.3. The velocity ranges of the four clouds in each panel is determined from the v - b diagram plotted in Figure 10(b). As already presented in Figure 6, the arch-like CO structure in the 50 km s^{-1} cloud in Figure 9(a) is spatially correlated with the bright $8 \mu\text{m}$ emissions, which consist of a network of the filamentary

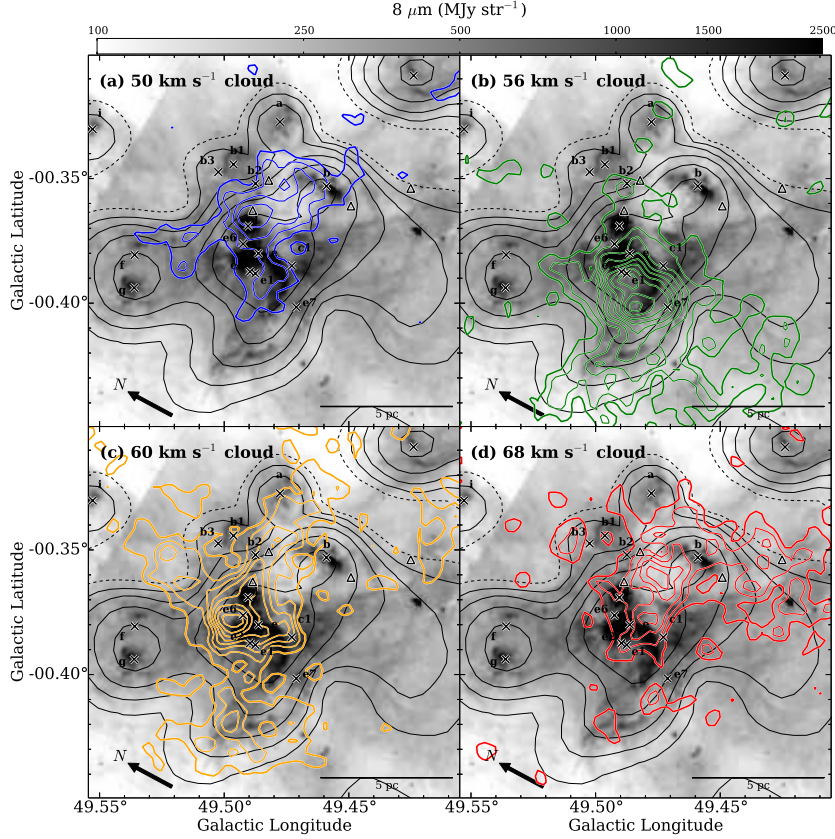


Fig. 7: C^{18}O ($J=1-0$) integrated intensity distributions of the four velocity clouds in G49.5-0.4 are presented as colored contour maps superimposed on the *Spitzer* $8\ \mu\text{m}$ image (Carey et al. 2009). The colored contours are plotted at every $2\ \text{K km s}^{-1}$ from $3\ \text{K km s}^{-1}$. The HII regions listed in Table 1 are depicted by crosses, and the massive young stars identified by Saral et al. (2017) are plotted with triangles. The black contours show the 21 cm continuum emissions plotted at the same levels as those in Figure 3.

structures elongated nearly parallel or perpendicular to the galactic plane. The $8\ \mu\text{m}$ filaments include the HII regions G49.4-0.3a, b, c, d, and e (see Table 1) and MYSOs. G49.4-0.3a, b and e out of them are spatially coincident with the $50\ \text{km s}^{-1}$ cloud, as discussed by Kang et al. (2010).

The $56\ \text{km s}^{-1}$ cloud in Figure 9(b) shows diffuse ^{13}CO emissions around the footpoints of the arch-like structure. In addition, there are three CO components, which appear to surrounding the 21 cm counters of G49.4-0.3, at $(l, b) \sim (49^\circ32, -0^\circ25)$, $(49^\circ33, -0^\circ36)$, and $(40^\circ46, -0^\circ31)$. In Figure 9(c) the filamentary structures of the $60\ \text{km s}^{-1}$ cloud shown in Figure 4(c) are plotted. The $8\ \mu\text{m}$ filaments stretched nearly parallel to the Galactic plane is traced by the upper-rim of the ^{13}CO filamentary structure of the $60\ \text{km s}^{-1}$ cloud at $l \sim 49^\circ34-49^\circ43$ and $b \sim -0^\circ32--0^\circ30$. The ^{13}CO filamentary structure harbors high- R_{3210}^{13} gas at the same l range, as shown in Figure 6. The $68\ \text{km s}^{-1}$

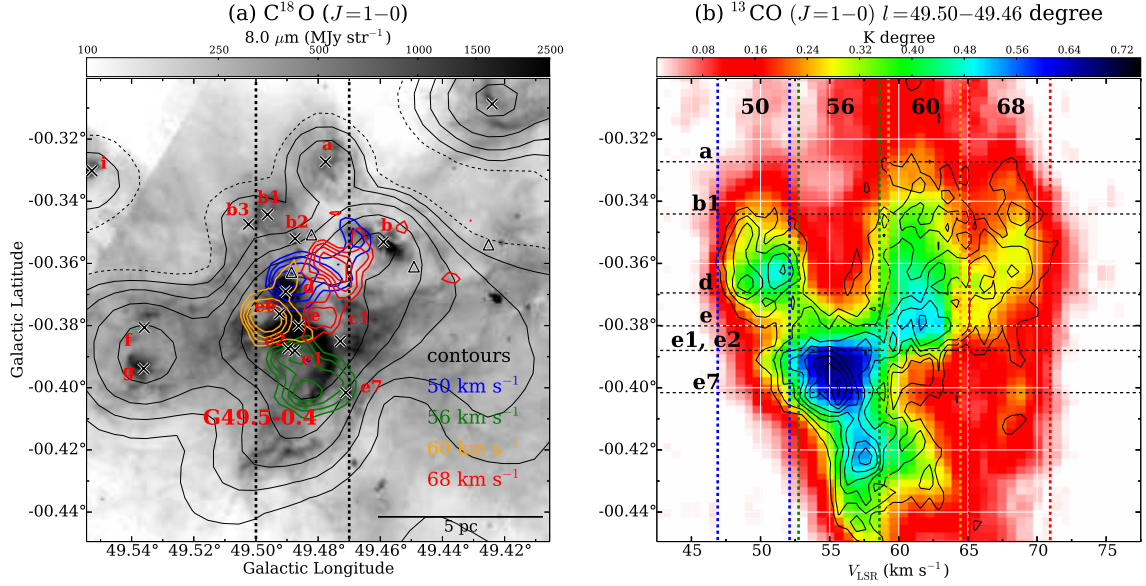


Fig. 8: (a) The contour maps of the $C^{18}O$ emissions of the four clouds around G49.5-0.4 are plotted superimposed on the *Spitzer* $8\mu m$ image and 21 cm contour map. The $C^{18}O$ contours are plotted at 60, 70, 80, and 90 % of the peak intensities of the four clumps. (b) Velocity–Galactic Latitude (v – b) diagram of the ^{13}CO (color) and $C^{18}O$ emissions (contours) towards G49.5-0.4 integrated over $l = 49^{\circ}50$ – $49^{\circ}46$, where the contours are plotted at every 0.03 K degree from 0.03 K degree. Horizontal dashed lines indicate the positions of compact HII regions, while the vertical dashed lines show the integration ranges of the four clouds presented in Figures 7 and 8(a).

cloud (HVS) in Figure 9(d) are distributed almost parallel to the filamentary structure in the 60 km s^{-1} cloud.

Figures 10(a) presents the $C^{18}O$ distributions of the four clouds toward G49.4-0.3 in the same manner as in Figure 8(a). While the 56 km s^{-1} cloud is not detected in $C^{18}O$, the 60 and 68 km s^{-1} clouds show fragmented distribution at $l \sim 49^{\circ}34$ – $49^{\circ}40$, and are aligned along the Galactic latitude with the 50 km s^{-1} cloud, showing a complementary distribution. The v – b diagram for this l range is presented in Figure 10(b), which shows that the 60 and 68 km s^{-1} clouds are bridged by the $C^{18}O$ emissions at the intermediate velocities, while the 50 and 60 km s^{-1} clouds are connected with the ^{12}CO emissions at $b \sim -0^{\circ}32$ – $-0^{\circ}29$ in 55 – 60 km s^{-1} , where the spatial distribution of the latter connecting feature is shown in Figure 9(b) in ^{13}CO . These intermediate velocity features may be interpreted as the broad bridge features which suggest interactions between different velocity components. Compared to the $8\mu m$ emissions in Figure 10(a), the $C^{18}O$ emissions of the 60 and 68 km s^{-1} clouds correspond to the regions with extinction in $8\mu m$, suggesting that these two clouds are both

located in front of the nebulosities of G49.4-0.3 (Ginsburg et al. 2015), lending another support to that these two clouds are distributed at the same location. At the top of the arch-like structure of the 50 km s^{-1} cloud, where G49.4-0.3a and several MYSOs are distributed, we cannot find complementary distribution among different velocity components, while there is possibly a bridge feature in the ^{12}CO emissions between the 50 and 60 km s^{-1} at $b \sim -0.24$ (Figure 8(b)).

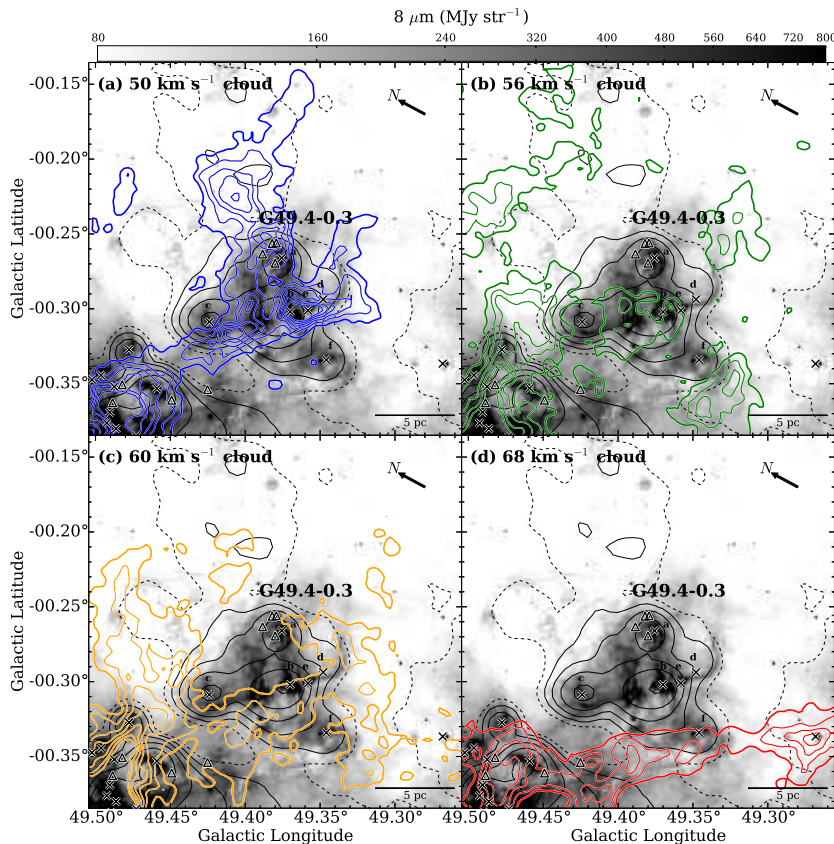


Fig. 9: ^{13}CO ($J=1-0$) integrated intensity distributions of the four velocity clouds in G49.4-0.3 are presented as colored contour maps superimposed on the *Spitzer* $8 \mu\text{m}$ image (Carey et al. 2009). Velocity ranges of the ^{13}CO emissions in the panels (a)–(d) are $47.2\text{--}54.4$, $55.7\text{--}58.3$, $59.6\text{--}64.1$, and $65.4\text{--}70.6 \text{ km s}^{-1}$, and contours are plotted at every 8 K km s^{-1} from 18 K km s^{-1} , every 4 K km s^{-1} from 4 K km s^{-1} , every 6 K km s^{-1} from 12 K km s^{-1} , and every 8 K km s^{-1} from 18 K km s^{-1} , respectively. Black contours show the 21 cm emissions plotted at the same levels as those in Figure 3. The HII regions listed in Table 1 are depicted by crosses, and the MYSOs identified by Saral et al. (2017) are plotted with triangles.

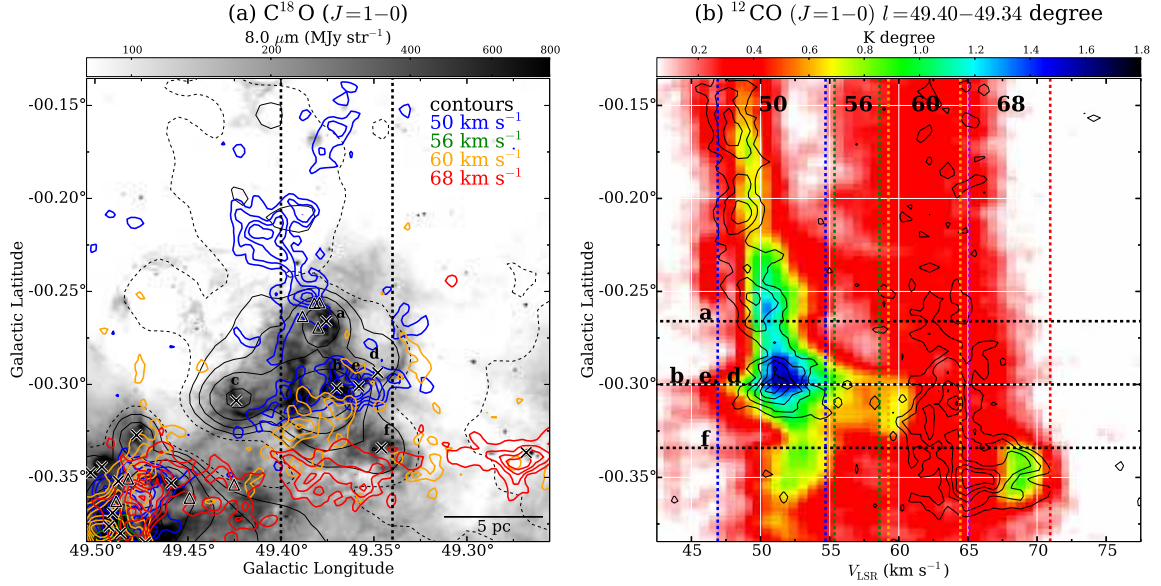


Fig. 10: (a) The colored contour maps (blue, green, orange, and red) of the C^{18}O emissions of the four clouds around G49.4-0.3 are plotted superimposed on the *Spitzer* $8\mu\text{m}$ image and 21 cm contour map (black). C^{18}O contours are plotted at every 2 K km s^{-1} from 4 K km s^{-1} . Crosses represent compact HII regions listed in Mehringer (1994) (Table 1), while the MYSO identified by Saral et al. (2017) is plotted with triangle. (b) Velocity–Galactic Latitude (v – b) diagram of ^{12}CO ($J=1-0$) integrated over $l = 49^{\circ}:40-49^{\circ}:34$. Contours indicate the C^{18}O ($J=1-0$) emissions and are plotted at every 0.02 K degree from 0.02 K degree . Horizontal dashed lines indicate the positions of compact HII regions, while the vertical dashed lines show the integration ranges of the four clouds presented in Figures 9 and 10(a).

4.2.3 G49.57-0.27

As presented in Figure 6, G49.57-0.27 shows high R_{3210}^{13} in the 50 and 56 km s^{-1} clouds. G49.57-0.27 is an isolated compact HII region located at $(l, b) \sim (49^{\circ}:57, -0^{\circ}:27)$, whose ionizing photon flux measured from a 21 cm continuum map corresponds to a spectral type of B0 (see Table 1). Figure 11(a) shows the ^{13}CO ($J=1-0$) integrated intensity maps of the 50 and 56 km s^{-1} clouds in contours and color, respectively. The CO emission in the 50 km s^{-1} cloud shows a roughly circular distribution with a diameter of $\sim 3\text{ pc}$, and is spatially coincident with G49.57-0.27 depicted by cross in Figure 11(a). On the other hand, the 56 km s^{-1} cloud shows two components separated along the Galactic longitude, and the 50 km s^{-1} component is sandwiched by these two components, indicating a complementary distribution. In the l - v diagram in Figure 11(b), the 50 km s^{-1} component is connected with the two separated component in the 56 km s^{-1} cloud, showing a “V-shape” gas distribution in the ^{12}CO ($J=1-0$) emissions. As introduced in Section 2, detections of V-shape gas distribution in the p - v diagram

were reported in the several CCC regions (e.g., Fukui et al. 2017b; Ohama et al. 2017b; Hayashi et al. 2017; Torii et al. 2017b). Based on the synthetic CO observations performed by Haworth et al. (2015a) using the CCC model by Takahira et al. (2014), Fukui et al. (2017b) and Torii et al. (2017b) reproduced the V-shape gas distribution in the p - v diagram (see Figure 14 of Fukui et al. (2017b)), which resembles the present CO observations shown in Figure 11(a).

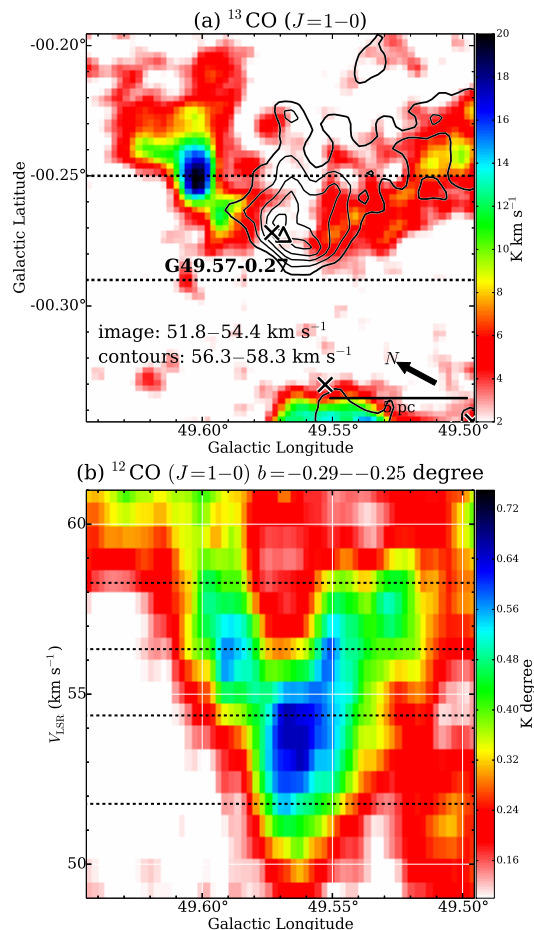


Fig. 11: (a) The complementary distributions of the two velocity components toward G49.57-0.27. The Color indicates $^{13}\text{CO} (J=1-0)$ for 56.3–58.3 km s^{-1} , while the contours show $^{13}\text{CO} (J=1-0)$ for 51.8–54.4 km s^{-1} . Contours are plotted at every 4 K km s^{-1} from 6 K km s^{-1} . Crosses represent compact HII regions listed in Mehringer (1994) (Table 1), while the MYSO identified by Saral et al. (2017) is plotted with triangle. (b) Galactic Longitude-velocity diagram of the $^{12}\text{CO} (J=1-0)$ emission toward G49.57-0.27. The integration range in b is shown in (a) with vertical dashed lines.

5 Discussion

Our analyses on the new CO ($J=1-0$) data basically confirmed the observed features in the previous studies by Carpenter & Sanders (1998) and Okumura et al. (2001). In addition, our CO data including the $C^{18}O$ ($J=1-0$) emission revealed previously unreported signatures that can be summarized as follows:

1. At the center of G49.5-0.4, in which IRS 1 and IRS 2 are located, the four $C^{18}O$ clumps, which are each embedded within the four velocity clouds, show a complementary distribution within a small area less than 5 pc. These are connected with each others in the $p-v$ diagram with ^{13}CO and/or $C^{18}O$ emissions, suggesting broad bridge features.
2. In G49.4-0.3, the ^{13}CO filamentary structures in the 50, 60, and 68 $km\ s^{-1}$ clouds elongated nearly parallel to the Galactic plane are aligned. These filamentary structures show high R_{3210}^{13} near G49.4-0.3, suggesting physical associations with G49.4-0.3. Each pair of the 50 and 60 $km\ s^{-1}$ clouds and the 60 and 68 $km\ s^{-1}$ clouds are connected with the bridge features in the $p-v$ diagram.
3. In the relatively evolved HII regions with larger sizes, i.e., G49.5-0.4f, g, h, and i, we found no CO counterparts which are spatially coincident with the HII regions along the line-of-sight, but identified the remnant CO fragments in the 50, 56, and 60 $km\ s^{-1}$ clouds, which have high R_{3210}^{13} at the rims of these HII regions.
4. In the isolated HII region G49.57-0.27, a complementary distribution between the gas components in the 50 and 56 $km\ s^{-1}$ clouds are discovered, where the circular CO emission in the 50 $km\ s^{-1}$ cloud is sandwiched by the two separated components in the 56 $km\ s^{-1}$ cloud. The complementary distribution is seen as a V-shape gas distribution in the $l-v$ diagram, which is well reproduced by the numerical calculation of CCC.

In this section, we discuss a CCC model in W51A based on the obtained results summarized above.

5.1 Ages of the HII regions

It is important to obtain the ages of the HII regions in W51A in order to discuss the formation mechanism of their exciting stars. Okumura et al. (2000) estimated the ages of the several HII regions listed in Table 1 by measuring sizes of the HII regions. We calculated the ages of the remaining HII regions using the analytical model of the D-type expansion developed by Spitzer (1978), where the sizes of the HII regions and classifications of the exciting sources summarized in Table 1 were adopted. We also assumed an uniform initial density of gas as $10^4\ cm^{-3}$, as the dense gas probed using $C^{18}O$ is widely detected in the molecular clouds in W51A. In Table 1 the ages estimated in this study are marked by asterisk.

5.2 CCC model in W51A

There are mainly two CCC models in W51A discussed in the previous studies by Carpenter & Sanders (1998) and Okumura et al. (2001). Carpenter & Sanders (1998) assumed that the present 50, 56 and 60 km s⁻¹ clouds, which correspond to 53, 58, 60, and 63 km s⁻¹ components in Carpenter & Sanders (1998), are inner-clouds of a single GMC (the W51 GMC). The authors discovered that the northern tip of the 68 km s⁻¹ cloud is truncated at the location of the 60 km s⁻¹ clouds. Although detailed process to create such a complementary distribution was not discussed, Carpenter & Sanders (1998) postulated a CCC scenario between these the W51 GMC and the 68 km s⁻¹ cloud.

On the other hand, based on the ¹³CO ($J=1-0$) observations in G49.5-0.4, Okumura et al. (2001) discussed CCCs for two pairs of the clouds, i.e., the 56 and 60 km s⁻¹ clouds and the 60 and 68 km s⁻¹ clouds. Although the authors did not find plausible evidence of the collision between the 50 and 56 km s⁻¹ clouds, they postulated a CCC model that four discrete molecular clouds distributed in a line along the line-of-sight are moving at different velocities, resulting in “pileup” of these four clouds.

Our results provide new insight into the CCCs in the W51A region. Figure 8(a) indicates that the 50, 56, 60, and 68 km s⁻¹ clouds show a complementary distribution. As introduced in Section 2, the recent works on CCC indicate that a complementary distribution can be created through a collision of two molecular clouds with different sizes or with a spatial offset (Torii et al. 2011; Fukui et al. 2017b). If so, the present results suggest that multiple collisions of the four clouds have occurred in G49.5-0.4, resulted in the formation of the massive stars at the interfaces of the collisions. In this scenario, it is reasonably assumed that the observed C¹⁸O clumps were formed through strong compression by the collisions. That the several compact HII regions are concentrated around the interfaces of the complementary distribution lends more credence to this CCC scenario. The timescale of CCC can be approximately estimated from a ratio of the cloud size and the relative velocity between the two clouds. If we assume the sizes of the four clumps of ~ 2 pc (Table 3) and the relative velocities of 4–18 km s⁻¹, the estimated timescales of the collisions in G49.5-0.4 ranges 0.1–0.5 Myrs. These figures are consistent with the estimated ages of the HII regions distributed around the interfaces of the complementary distribution, which include IRS 1 and IRS 2 (Table 1). While our results indicate that the 50, 56, and 60 km s⁻¹ clouds are almost blended within a small volume, which is consistent with the discussion by Ginsburg et al. (2015) based on the H₂CO absorption observations, spatial correlation of the 68 km s⁻¹ cloud with the extinction in the 8 μ m emission (see Figure 7(d)) shows that it is located in front of G49.5-0.4, not blended with the other three clouds.

G49.5-0.4 include relatively evolved HII regions with ages of a few Myrs, i.e., G49.5-0.4f,

g, h, and i (Table 1). As summarized in the beginning of this section, the remnant CO components of these HII regions are found in the 50, 56, and 60 km s⁻¹ clouds. These observed signatures can be interpreted as a CCC scenario or expansion of the HII regions. In the evolved HII regions, the complementary distribution and bridge features are dissipated and cannot be observed. Therefore it is difficult in the present study to conclude whether the exciting massive stars in these HII regions were formed via CCCs or not. If we tentatively assume that these HII regions were also formed via the collisions among these three clouds, the collisions should have occurred since a few Myrs ago. The sequential collisions and star formation from the north to the south are consistent with the discussion by Okumura et al. (2001).

In G49.4-0.3, the complementary distribution of gas and presence of the bridge features suggest collisions of the 50 and 60 km s⁻¹ clouds and the 60 and 68 km s⁻¹ clouds (Figure 10). As the filamentary structures in the 60 km s⁻¹ cloud look surrounding the 21 cm continuum emissions of G49.4-0.3 (Figure 4(c)), it is also possible to interpret that the associations of the multiple velocity components in G49.4-0.3 are due to expansion of the HII regions. If so, as the 60 km s⁻¹ cloud is redshifted relative to the systemic velocity of the HII regions in G49.4-0.3 having velocities of ~ 52 km s⁻¹ (Ginsburg et al. 2015), it should be located behind G49.4-0.3. However, as seen in Figure 10(a), the C¹⁸O components in the 60 km s⁻¹ cloud coincides with the extinction in the 8 μ m image. This indicates that it is located in front of G49.4-0.3 (Ginsburg et al. 2015), against for the assumption of the HII region expansion. On the other hand, in the CCC scenario, the bridge feature in the p - v diagram indicates that the collision is on-going, and it is possible that the 60 km s⁻¹ cloud has not completely passed over G49.4-0.3 along the line-of-sight yet. In the CCC scenario, the dissipative effect of the HII regions still can work on the 60 km s⁻¹ cloud to form CO components which surround G49.4-0.3 (Figure 4(c)), suggesting that the 60 km s⁻¹ cloud originally had an extended gas distribution in this region.

The timescale of the collision between the 50 and 60 km s⁻¹ cloud in G49.4-0.3 can be estimated as 0.2–0.6 Myr by assuming collision length ranging from the width of the filamentary structure, ~ 2 pc, to the full extension of the HII regions in G49.4-0.3, ~ 6 pc. The derived figures are consistent with the ages of the HII regions in G49.4-0.3, suggesting that the collision triggered formation of massive stars in G49.4-0.3. On the other hand, as we found no plausible evidence of physical association between the 68 km s⁻¹ cloud and the HII regions in G49.4-0.3, it may be that the 60 and 68 km s⁻¹ clouds are in the beginning of the collision, and compressed dense gas is observed in C¹⁸O as shown in Figure 10(a). Detailed observational studies having higher spatial resolutions of less than 0.1 pc are required to investigate future massive star formation in the dense gas at the colliding part.

In G49.57-0.27, the V-shape gas distribution in the l - v diagram in Figure 11(b) may also be

interpreted by expansion of the HII region. However, as the size of G49.57-0.27, ~ 0.4 pc (Table 1), is much smaller than that of the 50 km s^{-1} component with 3 pc, the observed V-shape gas distribution cannot be attributed to expansion of the HII region. It is therefore more likely that the V-shape was formed through the CCC process. The timescale required for the 50 km s^{-1} cloud to completely punch the 56 km s^{-1} cloud can be estimated as $3 \text{ pc} / 3 \text{ km s}^{-1} \sim 1 \text{ Myr}$, much longer than the estimated age of the HII region of G49.57-0.27, less than 0.1 Myr (Table 1). As the broad bridge feature indicates that the collision is still continuing, the collision in G49.57-0.27 is likely in the middle, which is consistent with the young age of G49.57-0.27.

Summarizing the above discussions, the observational signatures of CCCs in G49.5-0.4, G49.4-0.3 and G49.57-0.27 represent the collisions which have started since a few 0.1 Myr ago. This indicates that the four velocity components in this region, i.e., the 50, 56, 60, and 68 km s^{-1} clouds, are currently distributed close to each others, and are partly blended into one single molecular cloud. This is against for the assumption by Okumura et al. (2001) that the four clouds are located in a line along the line-of-sight. However, in the latter evolutionary stage of their “pileup” scenario, it can be expected that the four clouds are completely merged into a single cloud (see Figure 5 of Okumura et al. 2001). In this sense, our results are consistent with their CCC scenario. On the other hand, our results are also consistent with the discussion by Carpenter & Sanders (1998) that the 50, 56, and 60 km s^{-1} clouds represent kinematic structure within a single molecular cloud, as the total molecular mass in W51 is consistent with its virial mass for 100 pc scale, suggesting that self-gravity will play a critical role in the evolution of the molecular clouds in W51. In order to fully understand the kinematics and interactions of molecular clouds in W51, which will allow us to investigate the future of this region, it is important to study W51B using the same CO dataset. We will work on this issue in a separate paper.

6 Summary

We carried out new ^{12}CO ($J=1-0$), ^{13}CO ($J=1-0$), and C^{18}O ($J=1-0$) observations toward W51A as a part of the FUGIN project with the Nobeyama 45-m telescope. These observations covered a large area of W51A ($1.4^\circ \times 1.0^\circ$) at an angular resolution of $20''$ (~ 0.5 pc). The main conclusions of the present study are summarized as follows;

1. Our CO data identified four discrete velocity clouds with sizes and masses of ~ 30 pc and $1.0-1.9 \times 10^5 M_\odot$ at radial velocities of 50, 56, 60, and 68 km s^{-1} in W51A. These four clouds mainly consist of the bright CO emissions toward the two bright HII region complexes G49.5-0.4 and G49.4-0.3 attached with the filamentary structures elongated for several tens pc.

2. Based on comparisons between our ^{13}CO ($J=1-0$) data and the archival *JCMT* ^{13}CO ($J=3-2$) data, it was revealed that all of these four clouds are physically associated with G49.5-0.4, while the three of the four, i.e., 50, 60, and 68 km s^{-1} clouds, are interacted with G49.4-0.3, as the ^{13}CO ($J=3-2$)/ ^{13}CO ($J=1-0$) intensity ratios in these clouds are increased higher than 1.0 near the HII regions. The LVG calculations indicate such high ratios can be attributed to high temperature gas heated by the massive stars in these regions. We also found that the isolated HII region G49.57-0.27 located $\sim 15 \text{ pc}$ north of G49.5-0.4 are associated with the 50 and 56 km s^{-1} clouds.
3. In each of these three HII regions G49.4-0.5, G49.4-0.3, and G49.25-0.27, we revealed that the multiple velocity components associated with the HII regions show the “spatially complementary distributions” on the sky and “broad bridge features” in the position-velocity diagrams. In particular, in G49.25-0.27 a combination of the complementary distribution and the bridge features represent a “V-shape” gas distribution in the position-velocity diagram. These signatures have been discussed as the observational signatures of CCC in the recent theoretical and observational studies in the galactic HII regions.
4. We estimated the timescales of the collisions in these three regions to be several 0.1 Myrs by calculating crossing times of the collisions. These estimates are consistent with the ages of the HII regions measured from the sizes of the HII regions with the 21 cm continuum map.
5. Our present results lends more credence to the CCC scenario in W51A, that multiple velocity components have been continuously colliding with each others, resulting in active massive star formation in W51A.

Acknowledgments

This study was financially supported by Grants-in-Aid for Scientific Research (KAKENHI) of the Japanese society for the Promotion of Science (JSPS; grant numbers 15K17607). The authors would like to thank the all members of the 45-m group of Nobeyama Radio Observatory for support during the observation. Data analysis was carried out on the open use data analysis computer system at the Astronomy Data Center (ADC), of the National Astronomical Observatory of Japan (NAOJ), and made use of Astropy, a community-developed core Python package for Astronomy (Astropy Collaboration, 2013) and APLpy, an open-source plotting package for Python (Robitaille and Bressert, 2012). The authors also would like to thank NASA, National Radio Astronomy Observatory (NRAO), and Dr. H. Parsons for providing FITS data of *Spitzer* Space Telescope and *JCMT*, VGPS, and respectively.

References

- Anathpindika, S. V. 2010, MNRAS, 405, 1431
- Arnal, E. M., & Goss, W. M. 1985, A&A, 145, 369
- Bieging, J. 1975, H II regions and related topics, 42, 443
- Bonnell, I. A., Bate, M. R., Clarke, C. J., & Pringle, J. E. 2001, MNRAS, 323, 785
- Bonnell, I. A., Vine, S. G., & Bate, M. R. 2004, MNRAS, 349, 735
- Burton, W. B. 1970, A&AS, 2, 291
- Burton, W. B., & Shane, W. W. 1970, The Spiral Structure of our Galaxy, 38, 397
- Carey, S. J., Noriega-Crespo, A., Mizuno, D. R., et al. 2009, PASP, 121, 76
- Carpenter, J. M., & Sanders, D. B. 1998, AJ, 116, 1856
- Dickman, R. L. 1978, ApJS, 37, 407
- Egan, M. P., Shipman, R. F., Price, S. D., et al. 1998, ApJL, 494, L199
- Elmegreen, B. G., & Lada, C. J. 1977, ApJ, 214, 725
- Frerking, M. A., Langer, W. D., & Wilson, R. W. 1982, ApJ, 262, 590
- Fukui, Y., Ohama, A., Hanaoka, N., et al. 2014, ApJ, 780, 36
- Fukui, Y., Harada, R., Tokuda, K., et al. 2015, ApJL, 807, L4
- Fukui, Y., Torii, K., Ohama, A., et al. 2016, ApJ, 820, 26
- Fukui, Y., Tsuge, K., Sano, H., et al. 2017, PASJ, 69, L5
- Fukui, Y., Torii, K., Hattori, Y., et al. 2017, arXiv:1701.04669
- Fukui, Y., Kohno, M., Yokoyama, K., et al. 2017, arXiv:1706.05768
- Furukawa, N., Dawson, J. R., Ohama, A., et al. 2009, ApJL, 696, L115
- Ginsburg, A., Bally, J., Battersby, C., et al. 2015, A&A, 573, A106
- Goldader, J. D., & Wynn-Williams, C. G. 1994, ApJ, 433, 164
- Goldreich, P., & Kwan, J. 1974, ApJ, 189, 441

Goudis, C., & Hippelein, H. 1982, *A&A*, 105, 329

Habe, A., & Ohta, K. 1992, *PASJ*, 44, 203

Haworth, T. J., Shima, K., Tasker, E. J., et al. 2015, *MNRAS*, 454, 1634

Haworth, T. J., Tasker, E. J., Fukui, Y., et al. 2015, *MNRAS*, 450, 10

Hayashi, K., Sano, H., Enokiya, R., et al. 2017, arXiv:1706.05871

Hollenbach, D. J., & Tielens, A. G. G. M. 1999, *Reviews of Modern Physics*, 71, 173

Hosokawa, T., Yorke, H. W., & Omukai, K. 2010, *ApJ*, 721, 478

Hou, L. G., & Gao, X. Y. 2014, *MNRAS*, 438, 426

Inoue, T., & Fukui, Y. 2013, *ApJL*, 774, L31

Inoue, T., Hennebelle, P., Fukui, Y., et al. 2017, arXiv:1707.02035

Jogler, T., & Funk, S. 2016, *ApJ*, 816, 100

Kang, M., Bieging, J. H., Povich, M. S., & Lee, Y. 2009, *ApJ*, 706, 83

Kang, M., Bieging, J. H., Kulesa, C. A., et al. 2010, *ApJS*, 190, 58

Kim, H., Nakajima, Y., Sung, H., Moon, D.-S., & Koo, B.-C. 2007, *Journal of Korean Astronomical Society*, 40, 17

Kobayashi, M. I. N., Kobayashi, H., Inutsuka, S.-i., & Fukui, Y. 2017, arXiv:1708.07952

Kohno, M., Torii, K., Tachihara, K., et al. 2017, arXiv:1706.07964

Koo, B.-C., Kim, K.-T., & Seward, F. D. 1995, *ApJ*, 447, 211

Koo, B.-C. 1997, *ApJS*, 108, 489

Koo, B.-C., & Moon, D.-S. 1997, *ApJ*, 475, 194

Koo, B.-C., & Moon, D.-S. 1997, *ApJ*, 485, 263

Koo, B.-C. 1999, *ApJ*, 518, 760

Kumar, M. S. N., Kamath, U. S., & Davis, C. J. 2004, *MNRAS*, 353, 1025

Kuno, N., et al. 2011, *General Assembly and Scientific Symposium, XXXth URSI, JP2-19*

Leung, C.-M., & Liszt, H. S. 1976, *ApJ*, 208, 732

Leung, C. M., Herbst, E., & Huebner, W. F. 1984, *ApJS*, 56, 231

McKee, C. F., & Tan, J. C. 2003, *ApJ*, 585, 850

Mehring, D. M. 1994, *ApJS*, 91, 713

Minamidani, T., Nishimura, A., Miyamoto, Y., et al. 2016, *Proc. SPIE*, 9914, 99141Z

Moon, D.-S., & Park, Y.-S. 1998, *MNRAS*, 296, 863

Nagayama, T., Omodaka, T., Handa, T., et al. 2011, *PASJ*, 63, 719

Nishimura, A., Minamidani, T., Umemoto, T., et al. 2017a, arXiv:1706.06956

Nishimura, A., Costes, J., Inaba, T., et al. 2017b, arXiv:1706.06002

Ohama, A., Dawson, J. R., Furukawa, N., et al. 2010, *ApJ*, 709, 975

Ohama, A., Kono, M., Tsutsumi, D., et al. 2017, arXiv:1706.05659

Ohama, A., Tsutsumi, D., Sano, H., et al. 2017, arXiv:1706.05652

Oka, T., Nagai, M., Kamegai, K., Tanaka, K., & Kuboi, N. 2007, PASJ, 59, 15

Okumura, S.-i., Mori, A., Nishihara, E., Watanabe, E., & Yamashita, T. 2000, ApJ, 543, 799

Okumura, S.-I., Miyawaki, R., Sorai, K., Yamashita, T., & Hasegawa, T. 2001, PASJ, 53, 793

Pankonin, V., Payne, H. E., & Terzian, Y. 1979, A&A, 75, 365

Parsons, H., Thompson, M. A., Clark, J. S., & Chrysostomou, A. 2012, MNRAS, 424, 1658

Reid, M. J., Menten, K. M., Zheng, X. W., et al. 2009, ApJ, 700, 137-148

Rengarajan, T. N., Cheung, L. H., Fazio, G. G., Shivanandan, K., & McBreen, B. 1984, ApJ, 286, 573

Saral, G., Hora, J. L., Audard, M., et al. 2017, ApJ, 839, 108

Sano, H., Enokiya, R., Hayashi, K., et al. 2017, arXiv:1706.05763

Sato, M., Reid, M. J., Brunthaler, A., & Menten, K. M. 2010, ApJ, 720, 1055

Sawada, T., Ikeda, N., Sunada, K., et al. 2008, PASJ, 60, 445

Schneider, N., Bontemps, S., Motte, F., et al. 2016, A&A, 587, A74

Shimajiri, Y., Kitamura, Y., Saito, M., et al. 2014, A&A, 564, A68

Shimoikura, T., Dobashi, K., Saito, H., et al. 2013, ApJ, 768, 72

Shu, F. H., Adams, F. C., & Lizano, S. 1987, ARA&A, 25, 23

Solomon, P. M., Rivolo, A. R., Barrett, J., & Yahil, A. 1987, ApJ, 319, 730

Spitzer, L. 1978, Physical processes in the interstellar medium, by Lyman Spitzer. New York Wiley-Interscience, 1978. 333 p.,

Stil, J. M., Taylor, A. R., Dickey, J. M., et al. 2006, AJ, 132, 1158

Takahira, K., Tasker, E. J., & Habe, A. 2014, ApJ, 792, 63

Takahira, K., Shima, K., Tasker, E. J., & Habe, A. 2017, arXiv:1706.08656

Tan, J. C., Beltrán, M. T., Caselli, P., et al. 2014, Protostars and Planets VI, 149

Tian, W. W., & Leahy, D. A. 2013, ApJL, 769, L17

Torii, K., Enokiya, R., Sano, H., et al. 2011, ApJ, 738, 46

Torii, K., Hasegawa, K., Hattori, Y., et al. 2015, ApJ, 806, 7

Torii, K., Hattori, Y., Hasegawa, K., et al. 2017, ApJ, 835, 142

Torii, K., Hattori, Y., Matsuo, M., et al. 2017, arXiv:1706.07164

Tsuboi, M., Miyazaki, A., & Uehara, K. 2015, PASJ, 67, 109

Tsutsumi, D., Ohama, A., Okawa, K., et al. 2017, arXiv:1706.05664

Umemoto, T., Minamidani, T., Kuno, N., et al. 2017, arXiv:1707.05981

Vallée, J. P. 2014, ApJS, 215, 1

Wang, P., Li, Z.-Y., Abel, T., & Nakamura, F. 2010, ApJ, 709, 27

Westerhout, G. 1958, *Bull. Astron. Inst. Netherlands*, 14, 215
White, R. E. 1977, *ApJ*, 211, 744
Wilson, T. L., & Rood, R. 1994, *ARA&A*, 32, 191
Wolfire, M. G., & Cassinelli, J. P. 1987, *ApJ*, 319, 850
Wynn-Williams, C. G., Becklin, E. E., & Neugebauer, G. 1974, *ApJ*, 187, 473
Yorke, H. W., & Sonnhalter, C. 2002, *ApJ*, 569, 846
Zinnecker, H., & Yorke, H. W. 2007, *ARA&A*, 45, 481

Appendix 1 Velocity channel maps of the CO ($J=1-0$) emissions

In Figure 12, we presented velocity channel maps of the ^{12}CO ($J=1-0$), ^{13}CO ($J=1-0$) and C^{18}O ($J=1-0$) emissions at a velocity step of $\sim 3.3 \text{ km s}^{-1}$.

Appendix 2 Large velocity gradient analysis

In order to investigate high-temperature gas in the molecular clouds of W51A, we utilize the large velocity gradient (LVG) calculations (e.g., Goldreich & Kwan 1974). The assumption of the uniform velocity gradient is not always valid in the molecular gas associated with HII regions. However radiative transfer calculations assuming a micro-turbulent cloud interacting with an HII region shows no significant difference from the LVG analysis (e.g., Leung & Liszt 1976; White 1977). We therefore adopt the LVG approximation in the present study. We here adopted the abundance ratios of $[\text{C}^{12}\text{CO}]/[\text{C}^{13}\text{CO}] = 77$ (Wilson & Rood 1994) and the fractional CO abundance to be $X(\text{CO}) = [\text{C}^{12}\text{CO}]/[\text{H}_2] = 10^{-4}$ (e.g., Frerking et al. 1982; Leung et al. 1984). Two velocity gradient dv/dr of 5 and 10 $\text{km s}^{-1} \text{ pc}^{-1}$ were adopted, by assuming a typical velocity width of individual velocity clouds, $\sim 3 \text{ km s}^{-1}$ and a full velocity width of the four velocity clouds, $\sim 30 \text{ km s}^{-1}$ (see Figure 2), multiplied by a typical size of the molecular gas components of $\sim 3 \text{ pc}$.

Figure 15 shows R_{3210}^{13} distributions calculated with LVG for different densities $n(\text{H}_2)$ as a function of kinetic temperature T_k of gas, indicating that R_{3210}^{13} is sensitive to gas temperature. In all the $n(\text{H}_2)$ cases, R_{3210}^{13} of higher than 1.0 corresponds to T_k of higher than $\sim 20 \text{ K}$. 20 K is significantly higher than typical temperature of molecular clouds without star formation, 10 K (Fukui et al. 2016).

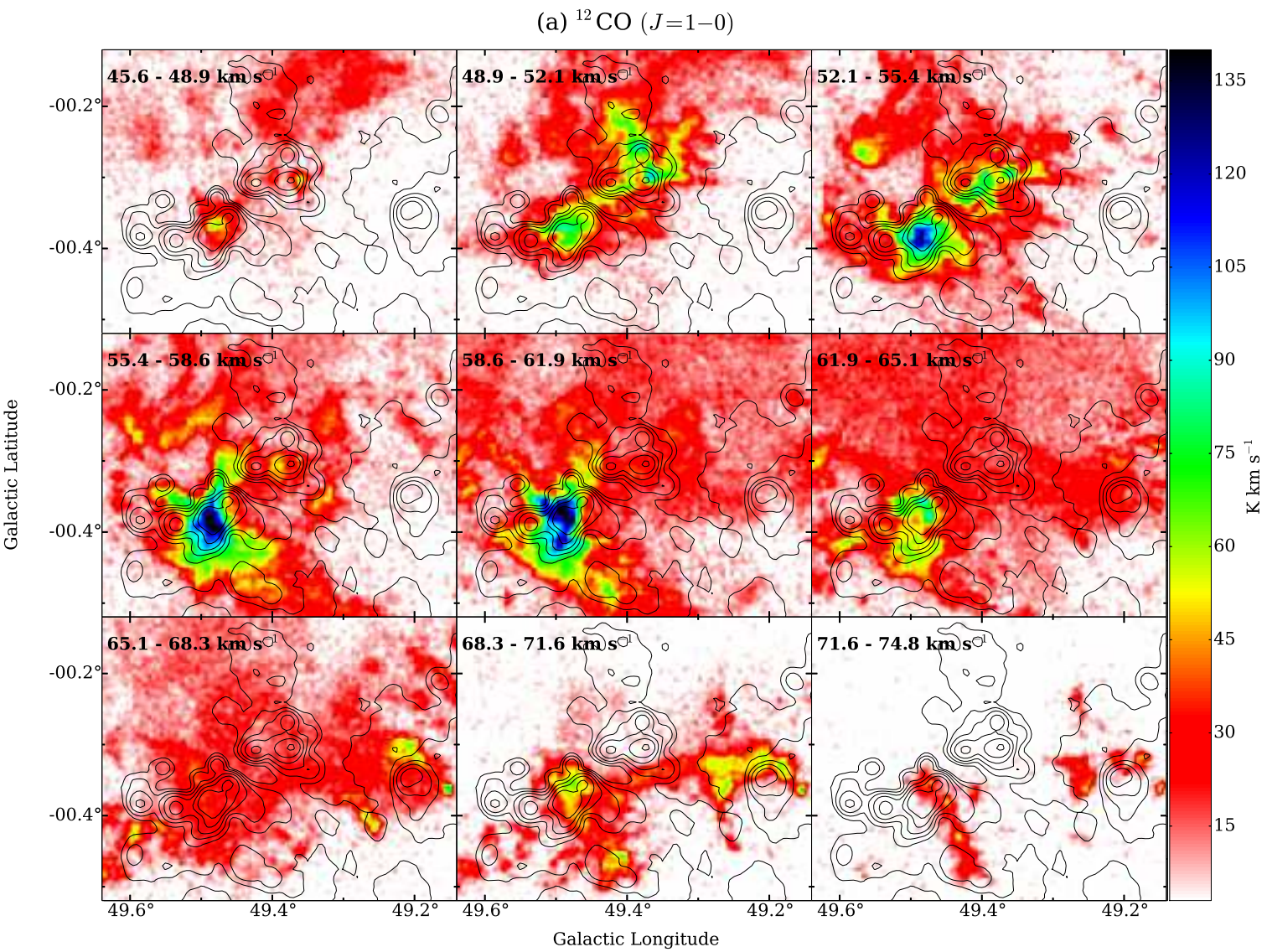


Fig. 12: The velocity channel maps of the ^{12}CO ($J=1-0$) emissions. Integration range in each panel is presented in the top-left corner of the panel. Black contours indicate the VGPS 21 cm radio continuum emission. Contour levels are 25 (thin lines), 50, 100, 200, 400 and 800 K. In these figures.

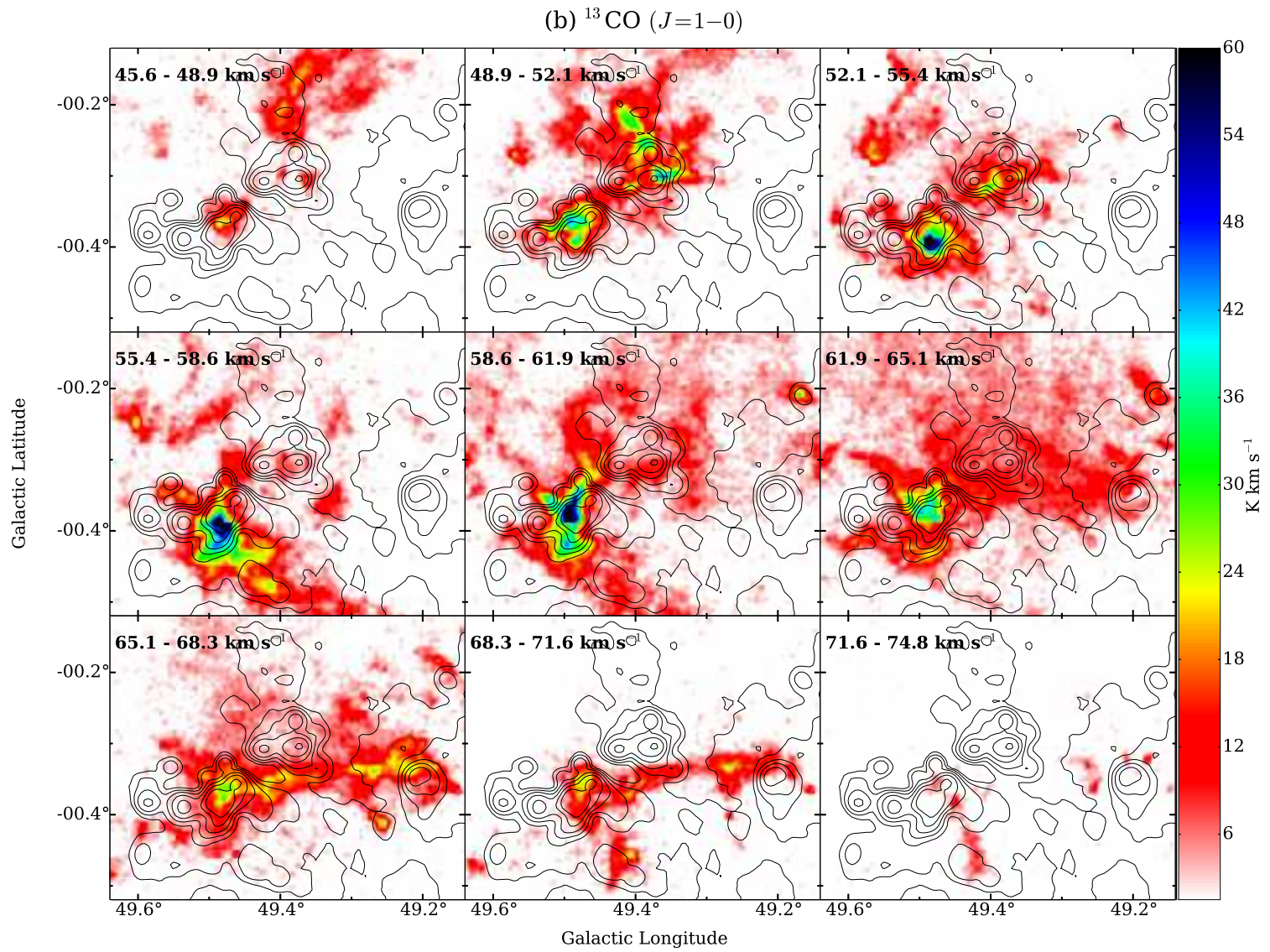


Fig. 13: Same as Fig. 12 but for ^{13}CO ($J=1-0$).

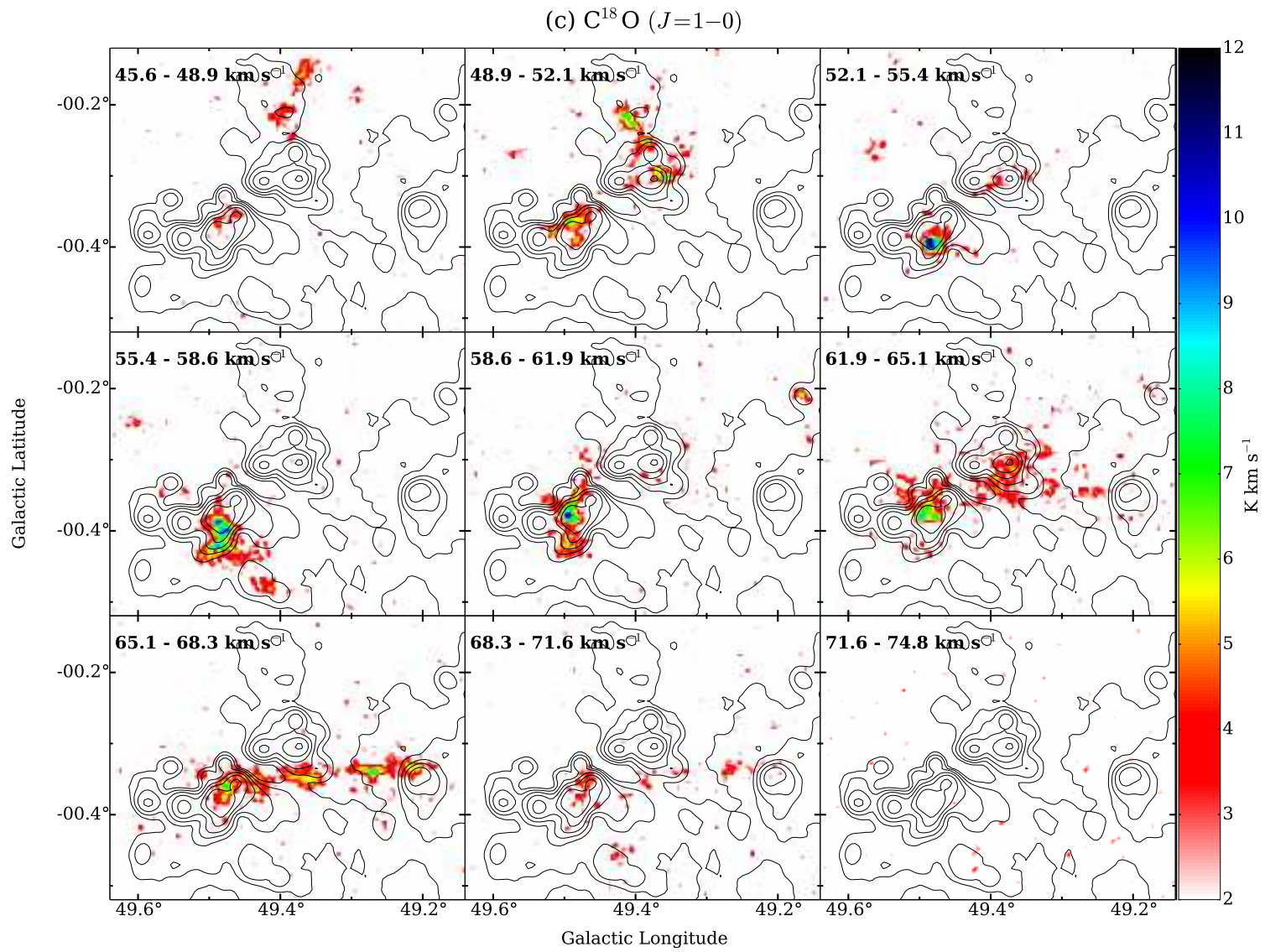


Fig. 14: Same as 12 but for C^{18}O ($J=1-0$).

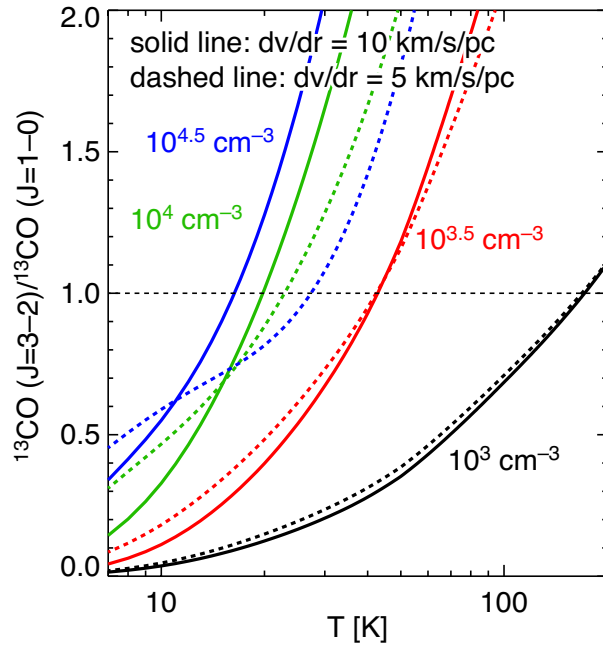


Fig. 15: Curves of R_{3210}^{13} as a function of T_k and $n(\text{H}_2)$, estimated using the LVG calculations. dv/dr is assumed $10 \text{ km s}^{-1} \text{ pc}^{-1}$ (solid lines) and $5 \text{ km s}^{-1} \text{ pc}^{-1}$ (dashed lines).